Chaos

Sliding homoclinic bifurcations in a Lorenz-type system: Analytic proofs

Cite as: Chaos **31**, 043117 (2021); https://doi.org/10.1063/5.0044731
Submitted: 19 January 2021 . Accepted: 22 March 2021 . Published Online: 15 April 2021

Vladimir N. Belykh, Nikita V. Barabash, and Igor V. Belykh

AIP Publishing

Chaos ARTICLE scitation.org/journal/cha

Sliding homoclinic bifurcations in a Lorenz-type system: Analytic proofs

Cite as: Chaos **31**, 043117 (2021); doi: 10.1063/5.0044731
Submitted: 19 January 2021 · Accepted: 22 March 2021 ·
Published Online: 15 April 2021

Vladimir N. Belykh,[1,2,a)] Nikita V. Barabash,[1,2,b)] and Igor V. Belykh[2,3,c)]

AFFILIATIONS

[1] Department of Mathematics, Volga State University of Water Transport, 5A Nesterov Str., Nizhny Novgorod 603950, Russia
[2] Department of Control Theory, Lobachevsky State University of Nizhny Novgorod, 23 Gagarin Ave., 603950 Nizhny Novgorod, Russia
[3] Department of Mathematics and Statistics, Georgia State University, P.O. Box 4110, Atlanta, Georgia 30302-410, USA

Note: This paper is part of the Focus Issue, Global Bifurcations, Chaos, and Hyperchaos: Theory and Applications.
[a)] **Electronic mail:** belykh@unn.ru
[b)] **Electronic mail:** barabash@itmm.unn.ru
[c)] **Author to whom correspondence should be addressed:** ibelykh@gsu.edu

ABSTRACT

Non-smooth systems can generate dynamics and bifurcations that are drastically different from their smooth counterparts. In this paper, we study such homoclinic bifurcations in a piecewise-smooth analytically tractable Lorenz-type system that was recently introduced by Belykh *et al.* [Chaos **29**, 103108 (2019)]. Through a rigorous analysis, we demonstrate that the emergence of sliding motions leads to novel bifurcation scenarios in which bifurcations of unstable homoclinic orbits of a saddle can yield stable limit cycles. These bifurcations are in sharp contrast with their smooth analogs that can generate only unstable (saddle) dynamics. We construct a Poincaré return map that accounts for the presence of sliding motions, thereby rigorously characterizing sliding homoclinic bifurcations that destroy a chaotic Lorenz-type attractor. In particular, we derive an explicit scaling factor for period-doubling bifurcations associated with sliding multi-loop homoclinic orbits and the formation of a quasi-attractor. Our analytical results lay the foundation for the development of non-classical global bifurcation theory in non-smooth flow systems.

In contrast to the well-established global bifurcation theory of smooth dynamical systems,[1–4] there is a critical gap in our understanding of non-local dynamics and bifurcations in piecewise-smooth systems. The celebrated Shilnikov saddle-focus[5] and saddle[6] theorems predict the emergence of global behavior in a smooth dynamical system from the local spectral properties. In particular, a positive saddle value induces the emergence of an unstable (saddle) periodic orbit from a homoclinic loop to a saddle equilibrium.[6] In this paper, we rigorously prove that a similar bifurcation in a piecewise-smooth analog of the Lorenz system[7] can lead to a remarkably different outcome and can generate a stable limit cycle due to the presence of sliding motions. Notably, the appearance of any small segment of sliding motions in an otherwise unstable homoclinic orbit can generate a stable periodic orbit. As a result, the emergence of these stable dynamics from multi-loop homoclinic orbits leads to the disappearance of a Lorenz-type attractor. Our rigorous description of "impossible" discontinuity-induced bifurcation scenarios contributes to the development of a universal suite of mathematical approaches that can transform our understanding of possible dynamics and structural changes of regular and chaotic attractors in systems with Filippov sliding motions.

I. INTRODUCTION

Non-smooth dynamics induced by switches, impacts, sliding, and other abrupt changes in system parameters are pervasive in physics, biology, and engineering.[8–10] In mechanics, non-smooth dynamical systems are used to model the dynamics of body interactions with non-smooth contact, impact, friction, and switching,[11,12] including pedestrian–bridge interactions[13–15] and vibro-impact energy harvesters.[16] In electrical and control engineering, non-smooth systems capture the dynamics of relay systems, switched power converters, and packet-switched networks.[11,17–20] In biology, non-smooth dynamics manifests in various systems, including gene regulatory networks[21,22] and pulse-coupled neurons.[23]

Such non-smooth dynamics are often modeled by piecewise-smooth systems whose phase space is partitioned into several regions with vector fields governed by different dynamical rules.[24] The introduction of discontinuity can induce a plethora of bifurcations, some with smooth counterparts, including fold-type or Andronov–Hopf-type bifurcations, but others are specifically associated with non-smooth phenomena such as grazing or sliding.[10,25–29] For example, limit cycles, tori, and chaotic attractors in piecewise-smooth dynamical systems can be born or disappear in ways fundamentally different from the smooth systems.[30–33] For example, there exist at least 20 different geometric mechanisms by which limit cycles can be created locally in a two-dimensional piecewise-smooth flow system.[34] The local Andronov–Hopf-like bifurcations underlying these mechanisms include boundary equilibrium bifurcations and limit cycles created from folds.[10]

The local bifurcation theory for piecewise-smooth systems with sliding motions is relatively well developed, especially for piecewise-smooth maps where jumps in multipliers induce border-collision bifurcations[35] (also known as C-bifurcations[36,37]) and non-smooth analogs of a Neimark–Sacker bifurcation.[31] At the same time, the global bifurcation theory of piecewise-smooth systems is in its infancy (see an excellent review of the state-of-the-art on discontinuity-induced bifurcations[38]). Most of the existing results deal with identifying the conditions under which global bifurcations in piecewise-smooth flow systems are similar to their classical counterparts in smooth systems.[39,40] These include a version of a Shilnikov saddle-focus theorem for Filippov systems where a sliding Shilnikov homoclinic loop to a pseudostationary focus yields countably infinitely many sliding saddle periodic orbits.[40] It was also qualitatively shown that sliding motions in a planar Filippov system can yield a sliding homoclinic bifurcation of a saddle in which a separatrix loop generates a stable limit cycle, independent from the sign of a saddle value.[30] However, generic conditions and properties of many other global discontinuity-induced bifurcations in three and higher dimensions are still an open problem. For example, piecewise-smooth systems can merge together saddle-focus homoclinic orbits with Filippov sliding motions and boundary equilibrium bifurcations, yielding a fundamentally new, complicated bifurcation set,[41] which calls for the development of new rigorous methods.

In this paper, we seek to close this gap by offering an exact description of sliding homoclinic bifurcations that lead to a scenario in which a bifurcation of an unstable homoclinic orbit can generate a stable (not a saddle) periodic orbit. In a recent work,[7] we proposed a method for designing piecewise-smooth dynamical systems with a predefined chaotic attractor and exact solutions that may open the door to the synthesis and rigorous analysis of hyperbolic attractors. This method was used to construct a simple piecewise-smooth model that switches between linear systems that yield a singular hyperbolic Lorenz-type attractor whose properties were described rigorously without any computer assistance. The integrability of the linear systems composing our model allowed for constructing an explicit Poincaré return map and rigorously proving the existence of a Lorenz-type attractor and explicitly characterizing bifurcations that lead to its birth and structural changes. Notably, a similar task of proving the existence of the original Lorenz attractor turned out to be a long-term existing challenge that was resolved only recently via computer-assisted methods[42] for the Lorenz system and via rigorous methods for an extended Lorenz system.[43] Similarly, the complex bifurcation structure of the original Lorenz system controlling the birth and disappearance of the Lorenz attractor was primarily studied via qualitative, computer-assisted, or numerical methods.[44–58]

The rigorous bifurcation analysis in our previous work[7] was performed for a set of parameters that guarantee that sliding motions are not part of the Lorenz-type attractor and, therefore, do not play a role in its formation. This paper offers a different vision that embraces and exploits non-smooth dynamics and sliding motions toward describing a novel type of discontinuity-induced homoclinic bifurcations that lead to the destruction of the Lorenz-type attractor. To account for the presence of sliding motions, we refine the Poincaré return map[7] so that stable sliding motions induce symmetric flat fragments in the map's graph. The appearance of these flat fragments results in significant changes in the bifurcation sequence that leads to the formation of the Lorenz-type chaotic attractor and also determines a bifurcation mechanism of its destruction. Extending our numerical study,[59] we rigorously prove that the Lorenz-type attractor in our piecewise-smooth system can be born in a fundamentally different way than in the original Lorenz system due to the presence of sliding motions. To do so, we depart from the classical, ground zero setting of the Lorenz system that corresponds to a parameter set, which only yields a saddle with a positive saddle value and two stable foci. We then prove that the formation of a classical homoclinic butterfly, which contains even an infinitesimal small piece of sliding motions or is simply tangent to the sliding manifold, results in the birth of a stable period-2 butterfly-shaped orbit. This is in stark contrast with the classical homoclinic butterfly bifurcation in the original smooth Lorenz system, which only generates a saddle orbit. We also show how changes caused by sliding motions generate a quasi-attractor via a sequence of period-doubling bifurcations associated with multi-loop homoclinic bifurcations. This sequence finally ends at the formation of the chaotic Lorenz-type attractor, which contains no sliding motions. Due to the analytical tractability of our piecewise-smooth system, we are able to indicate the parameter values that correspond to multi-loop bifurcations and to derive an explicit scaling factor for the period-doubling homoclinic bifurcations.

In terms of the smooth Lorenz-type systems, our analytically characterized bifurcation scenario resembles the routes to chaos studied qualitatively and numerically in Lorenz-type systems.[60,61] Common to these scenarios is the accumulation of period-doubling bifurcations due to the emergence of stable multi-loop homoclinic orbits. A crucial caveat that distinguishes our bifurcation scenario is that the homoclinic bifurcations that generate stable periodic orbits in the smooth Lorenz-type systems[60,61] correspond to the case of a negative saddle value, as required by the Shilnikov saddle theorem,[6] whereas our non-traditional bifurcation route to singular hyperbolic Lorenz-type chaos corresponds to a positive saddle value and is impossible in smooth systems.

The layout of this paper is as follows. First, in Sec. II, we review the main properties of our piecewise-smooth Lorenz-type model introduced in Ref. 7. These properties include the model construction, the phase space partition, the existence of an absorbing domain, and the description of possible sliding motions. In Sec. III, we construct a flow-defined two-dimensional (2D) Poincaré return map that accounts for the role of sliding motions in the formation and destruction of the Lorenz-type attractor. Like the original map introduced in our previous work,[7] this 2D map has a triangular form where a one-dimensional (1D) master map for the x variable drives the y component. In Sec. IV, we exploit this property by analyzing bifurcations and attractors in the 1D master map and connecting them to the bifurcation set of the piecewise-smooth flow system. In Sec. V, we explicitly describe the route to Lorenz-type chaos via an infinite sequence of multi-loop homoclinic bifurcations and derive the scaling factor. In Sec. VI, we conclude the study and offer a conjecture for the emergence of similar sliding bifurcations in other non-smooth systems.

II. THE PIECEWISE-SMOOTH MODEL

To reveal a new type of sliding homoclinic bifurcations in non-smooth systems, we consider a piecewise-smooth Lorenz-type system[7] that displays a singular hyperbolic strange attractor in the absence of sliding motions. We briefly discuss the system's structure and its main dynamical properties; more details can be found in Ref. 7. To facilitate the cross-paper reading, we keep the original notations when applicable.

A. Model structure and explicit solutions

Our piecewise-smooth system is composed of three-dimensional linear subsystems A_s, A_l, and A_r,

$$\begin{aligned}
A_s &: \quad \begin{array}{l} \dot{x} = x, \\ \dot{y} = -\alpha y, \\ \dot{z} = -\nu z, \end{array} \quad (x,y,z) \in G_s, \\
A_l &: \quad \begin{array}{l} \dot{x} = -\lambda(x+1) + \omega(z-b), \\ \dot{y} = -\delta(y+1), \\ \dot{z} = -\omega(x+1) - \lambda(z-b), \end{array} \quad (x,y,z) \in G_l, \\
A_r &: \quad \begin{array}{l} \dot{x} = -\lambda(x-1) - \omega(z-b), \\ \dot{y} = -\delta(y-1), \\ \dot{z} = \omega(x-1) - \lambda(z-b), \end{array} \quad (x,y,z) \in G_r,
\end{aligned} \tag{1}$$

where α, δ, ν, ω, λ, and b are positive parameters. These subsystems determine the system's vector flows in the following partitions of the system's phase space, G_s, G_l, and G_r, respectively:

$$\begin{aligned}
&G_s : |x| < 1, y \in \mathbb{R}^1, z < b, \\
&G_l : \begin{cases} x \le -1 & \text{for } z \le b, \\ x \le -1 & \text{for } z > b \quad \text{and} \quad y \ge 0, \\ x < 1 & \text{for } z > b \quad \text{and} \quad y < 0, \end{cases} \\
&G_r : \begin{cases} x \ge 1 & \text{for } z \le b, \\ x \ge 1 & \text{for } z > b \quad \text{and} \quad y < 0, \\ x > -1 & \text{for } z < b \quad \text{and} \quad y \ge 0. \end{cases}
\end{aligned} \tag{2}$$

Each of the linear subsystems has a unique fixed point. Subsystem A_s has a saddle fixed point O_s at the origin and determines the vector flow of system (1) in the saddle region G_s. Subsystems $A_{r,l}$ display symmetrical stable foci $e_{r,l} = \{\pm 1, \pm 1, b\}$ in the focus regions $G_{r,l}$, respectively. These two foci may become unstable in full piecewise-smooth system (1). In fact, trajectories in the vicinity of $e_{r,l}$ are comprised from the solutions of focus systems $A_{r,l}$ and saddle system A_s whose balance may favor overall stability or instability of $e_{r,l}$ when the parameters vary.

By construction, piecewise-smooth system (1) has several discontinuity boundaries at which the vector flow switches from one system to another. These are (i) vertical half-planes $S_1 = \{x = 1, y \in \mathbb{R}^1, z < b\}$, $S_2 = \{x = -1, y \in \mathbb{R}^1, z < b\}$, and the part of plane $D = \{|x| \le 1, y \in \mathbb{R}^1, z = b\}$ that bound saddle region G_s on the right, left, and above, respectively, and (ii) gray Z-shaped boundary Z_s that separates focus regions $A_{r,l}$ above plane D (see Fig. 1).

Trajectories of system (1) are glued from trajectories of subsystems A_s, A_l, and A_r that are available in the form of explicit analytical solutions. More specifically, a trajectory initiating from horizontal discontinuity section D with $z(0) = b$ is defined by saddle system A_s via

$$\begin{aligned}
x(t) &= x(0)\, e^{t}, \\
y(t) &= y(0)\, e^{-\alpha t}, \\
z(t) &= b\, e^{-\nu t}.
\end{aligned} \tag{3}$$

The solution of focus system A_r with initial conditions $x(0) = x_0 = 1$, $y(0) = y_0$, $z(0) = z_0$ on S_1 is defined by

$$\begin{aligned}
x(t) &= 1 + (b - z_0)\, e^{-\lambda t} \sin(\omega t), \\
y(t) &= 1 + (y_0 - 1)\, e^{-\delta t}, \\
z(t) &= b - (b - z_0)\, e^{-\lambda t} \cos(\omega t).
\end{aligned} \tag{4}$$

The solution of focus system A_l with initial conditions $x(0) = -1$, $y(0) = y_0$, $z(0) = z_0$ on S_2 has the form

$$\begin{aligned}
x(t) &= -1 - (b - z_0)\, e^{-\lambda t} \sin(\omega t), \\
y(t) &= -1 + (y_0 + 1)\, e^{-\delta t}, \\
z(t) &= b - (b - z_0)\, e^{-\lambda t} \cos(\omega t).
\end{aligned} \tag{5}$$

For example, the right blue trajectory of Fig. 1(a) starting from and returning to discontinuity section D contains two parts where the first part from D to the discontinuity half-plane S_1 is defined by saddle solution (3) and then continued from S_1 back to D by focus solution (4).

As in the original smooth Lorenz system, saddle O_s in system (1) has a two-dimensional stable manifold defined by W^s and one-dimensional unstable manifolds, defined by W^u_1 and W^u_2 (Fig. 1). Defined through saddle system A_s, written as a normal form of a saddle, the eigenvalues of O_s are $s_1 = 1$, $s_2 = -\alpha$, and $s_3 = -\nu$. Central to our study is the sign of the saddle value (also known as the saddle quantity) of saddle O_s determined as $\eta = s_1 + \max\{s_2, s_3\}$. We choose the parameters to satisfy the condition

$$1/2 < \nu < 1 < \alpha. \tag{6}$$

The choice of $\nu < 1 < \alpha$ guarantees that $s_3 = -\nu$ is the least negative eigenvalue, thereby making saddle value $\eta = 1 - \nu$ positive.

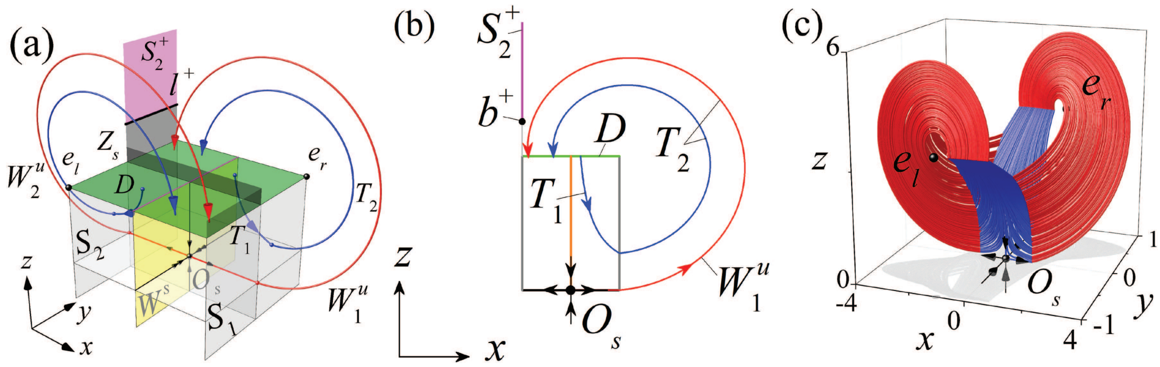

FIG. 1. Phase structure and dynamics of piecewise-smooth system (1) under no-sliding condition (10). (a) The box-shaped saddle region is bounded by vertical half-planes S_1 and S_2 (gray) and horizontal cross section D (green plane). The left and right focus regions are separated by the saddle region and Z-shaped section Z_s (dark green). Unstable manifold W_1^u of saddle O_s (red) cannot reach stable sliding half-plane S_2^+ (pink), thereby guaranteeing that the system's attractor contains no sliding motions. Typical trajectories (blue) starting from and returning to D are composed from the parts of the saddle and focal trajectories. (b) The xz projection of (a) with $y = 0$. The construction of map $F = T_2T_1$: the initial point on cross section D is transferred to half-plane S_1 (right gray vertical line) by the trajectory of the saddle system (map T_1) and then is returned back to D by the trajectory of the focus system (map T_2). Point $z = b^+$ indicates the lower border of stable sliding half-plane S_2^+, line l^+ (not shown). (c) The corresponding Lorenz-type attractor with no sliding motions. Chaotic trajectories are glued from pieces of saddle (blue) and focal (red) trajectories of three linear systems (3)–(5). The trajectories in all three plots are calculated numerically. Parameters are $\alpha = 2$, $\nu = 0.8$, $\lambda = 0.1471$, $\omega = 1$, $b = 3.6$, and $\delta = 0.588$.

It also ensures that plane $W^{lead} = ((x, z) \in G_s, y = 0)$ determines the leading (weaker) direction as a piece of leading stable manifold W^s, similarly to the original Lorenz system that displays the Lorenz attractor.[62] The choice $1/2 < \nu < 1$ in (6) determines the interval where a unique strange Lorenz-type attractor may exist (see Remark 2 in Ref. 7 for the details).

Like the original Lorenz system, piecewise-smooth system (1) is eventually dissipative and has an absorbing domain G that attracts all trajectories and contains all attractors of system (1). The explicit form of G and its derivation are given in Ref. 7.

B. Sliding motions

Stable sliding regions in piecewise-smooth system (1) are only located on the following parts of the Z-shaped discontinuity surface:[7,59]

$$\begin{aligned} S_1^+ &= \{x = 1, z > b^+ = b + 2a, y \in (-1, 0)\}, \\ S_2^+ &= \{x = -1, z > b^+ = b + 2a, y \in (0, 1)\}, \end{aligned} \tag{7}$$

where $a = \lambda/\omega$ is a new parameter to be used throughout the paper. The stability of sliding regions $S_{1,2}^+$ originates from the mutual arrangement of the x components of vector flows of systems A_r and A_l that are directed toward each other at S_1^+ and S_2^+. This arrangement changes on the extensions of S_1^+ and S_2^+ [dark gray region in Fig. 1(a)] from $z = b^+$ down to D, making them passable for the system's trajectories. By the same argument, the middle section of the Z-shaped discontinuity surface ($y = 0, |x| < 1, z \geq b$) contains only unstable sliding motions, rendering it unreachable.[7]

To analyze the directions of motion for sliding trajectories on stable half-planes $S_{1,2}^+$, we follow Filippov's approach[9] and define sliding motions on $S_{1,2}^+$ through the following (y, z) system:

$$\begin{aligned} \dot{y} &= \delta\left(-y + \frac{a}{z - b - a}\right), \\ \dot{z} &= -\omega\left[1 + a(z - b) + \frac{a}{z - b - a}\right]. \end{aligned} \tag{8}$$

This system represents the Filippov vector field $\dot{X} = F_F$ that defines equations of motion at a 2D sliding surface $S(X) = 0$ by

$$\dot{X} = F_F = \kappa(X)F_r(X) + (1 - \kappa(X))F_l(X), \tag{9}$$

where X is a coordinate vector, F_r and F_l are the vector fields separated by the sliding surface, and coefficient $\kappa(X)$ is defined by dot product $(F_F, \nabla S(X)) = 0$. In our case of sliding surfaces $S_{1,2}^+$, the F_r and F_l vector fields are represented by focus systems A_r and A_l, and the gradient of $S(X)$ at $S_{1,2}^+$ is vector $\nabla S(1, 0, 0)$. Therefore, combining (1)–(9) yields system (8). Note that both $z - b > 0$ and $z - b - a > 0$ at sliding half-planes $S_{1,2}^+$ [see (7)]. Therefore, $\dot{z} < 0$ in (8) and z decreases along $S_{1,2}^+$. As a result, all trajectories on stable sliding half-planes $S_{1,2}^+$ slide down along $S_{1,2}^+$ to reach the boundary $z = b^+$ and then leave the sliding half-planes.

In our previous work, we derived the following conditions on the system's parameters:

$$\begin{aligned} \delta &> \delta_{cr} = \frac{\omega \ln 2}{\pi}, \\ b &< b_{cr} = 2\sqrt{1 + a^2}\exp\left\{a\left(\arctan a^{-1} + \pi\right)\right\}, \end{aligned} \tag{10}$$

which guarantee that attractors of system (1) contain no sliding motions (see Theorem 1 in Ref. 7). In other words, the attractors' trajectories, including unstable manifolds W_1^u and W_2^u, cannot reach stable sliding half-planes $S_{1,2}^+$. As a result, stable sliding motions play no role in the system's dynamics, thereby allowing for the emergence of a singular hyperbolic Lorenz-type attractor with only saddle trajectories. This is the case depicted in Fig. 1(c).

In the following, we will analyze the dynamics of system (1) beyond parameter range (10) where the presence of sliding motions leads to the destruction of the Lorenz-type attractor via a cascade of non-traditional homoclinic bifurcations.

III. THE POINCARÉ RETURN MAP IN THE PRESENCE OF SLIDING MOTIONS

We seek to construct a flow-defined Poincaré return map that accounts for the presence of sliding motions and helps reveal their non-trivial role in the system's behavior and bifurcations. Toward this aim, we begin with an explicit Poincaré return map[7] previously derived for the vector flow of (1) under no-sliding condition (10). This Poincaré return map is constructed by choosing discontinuity section $D = \{|x| \le 1, |y| \le 1, z = b\}$ as a Poincaré cross section and analyzing how D is mapped into itself by trajectories of saddle (A_s) and focus systems $A_{r,l}$. By construction, D with $z = b$ is a global cross section that is analogous to the global cross section $z = \rho - 1$ in the original Lorenz system[45]

$$\dot{x} = \sigma(y - x), \quad \dot{y} = \rho x - y - xz, \quad \dot{z} = xy - \beta z. \tag{11}$$

A. The geometrical construction

Cross section D contains two symmetrical parts, $D_1 = D|_{x \ge 0}$ and $D_2 = D|_{x \le 0}$, separated by stable manifold W^s of O_s along intersection line $W^s \cap D$ [Fig. 2(a)]. Due to the system's symmetry, it is sufficient to derive map $F_1 : D_1 \to D$; map $F_2 : D_2 \to D$ is simply its odd-symmetrical complement.

In the absence of sliding motions, Poincaré return map F_1 is a composition of maps $T_1 : D_1 \to S_1$ and $T_r : S_1 \to D$. As illustrated in Figs. 1(a) and 1(b), map $T_1 : D_1 \to S_1$ transfers points from half-section D_1 to vertical half-plane S_1 along the trajectories of saddle system A_s. Then, map $T_2 : S_1 \to S_1$ brings these points back to cross section D by the trajectories of focus system A_r. Due to the integrability of linear systems A_s and A_r and their explicit solutions (3) and (4), Poincaré return map F_1 can be cast into the following explicit form:[7]

$$\begin{array}{ll} \bar{x} = f(x) \equiv 1 - \gamma + \gamma x^{\nu}, & \\ \bar{y} = g(x, y) \equiv 1 - r + r x^{\alpha} y, & \text{for } x > 0, \\ \bar{x} = f(x) \equiv \gamma - 1 - \gamma |x|^{\nu}, & \\ \bar{y} = g(x, y) \equiv r - 1 + r|x|^{\alpha} y, & \text{for } x < 0, \end{array} \tag{12}$$

where $\bar{x}$ ($\bar{y}$) indicates subsequent iterate x_{k+1} of x_k (y_{k+1} of y_k) under the action of F_1, and the new parameters are

$$\gamma = b\, e^{-\frac{3\pi\lambda}{2\omega}}, \quad r = e^{-\frac{3\pi\delta}{2\omega}}. \tag{13}$$

Further details on the properties of map F_1 and their rigorous analysis can be found in Ref. 7.

The main goal of this section is to modify map (12) to extend its applicability beyond no-sliding condition (10). In this case, unstable manifold W_1^s of saddle O_s reaches the stable sliding half-plane S_2^+ [the pink region in Fig. 2(a)] and slides down along S_2^+ before returning to cross section D [Figs. 2(a) and 2(b)]. As a result, there exists a region of initial conditions $D_1^{sl} \in D_1$ [the dark green area in Fig. 2(a)] for which the trajectories starting from D_1^{sl} fall on stable sliding half-plane S_2^+. The border of D_1^{sl} is composed of the initial conditions whose images land on the lower boundary of S_2^+, line $l^+ : \{x = -1, z = b^+, y > 0\}$ [the black line separating the pink and gray regions in Fig. 2(a)].

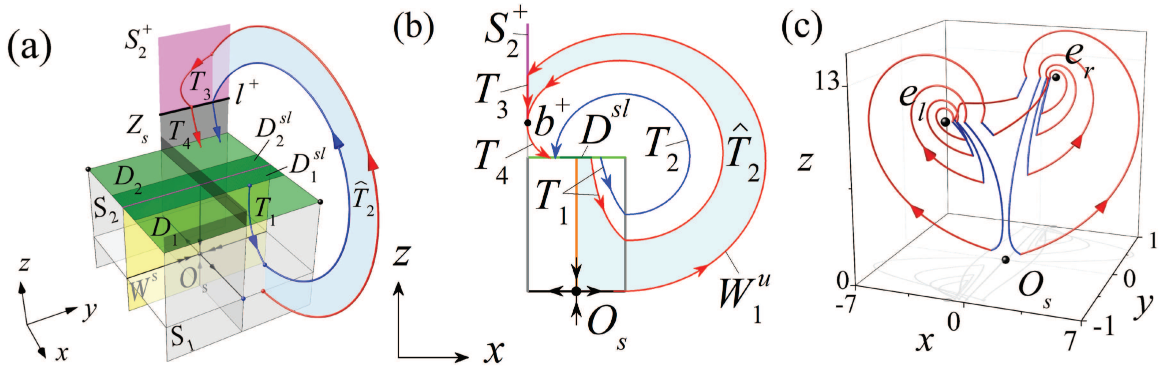

FIG. 2. Dynamics in the presence of stable sliding motions. (a) Trajectories starting from rectangular section D_1^{sl} reach stable sliding half-plane S_2^+ (pink region), slide down, and leave S_2^+ at l^+ to return back to cross section D. The strip (light blue) bounded by the blue and red trajectories indicates the possible coordinate range for such trajectories with stable sliding parts. Each trajectory from this range is made of four parts: the saddle part (map T_1), the focal part (map $\hat{T}_2$), the sliding part (map T_3), and another focal part (map T_4). (b) The xz slice of (a) with $y = 0$. Trajectories with initial conditions on D^{sl} (dark green line) bounded by two red trajectories and comprising the light blue strip yield map $\hat{F} = T_4 T_3 \hat{T}_2 T_1$. The blue trajectory starts from cross section D (light green line) but beyond D^{sl} and does not reach S_2^+; therefore, it generates non-sliding map $F = T_2 T_1$. (c) The emergence of stable sliding motions induces a stable multi-period orbit comprised from saddle (blue) and focal (red) parts. The trajectories in all three plots are calculated numerically. Parameters are $\alpha = 2$, $\nu = 0.8$, $\lambda = 0.3684$, $\omega = 1$, $b = 11.35$, and $\delta = 0.588$.

Therefore, we need to construct Poincaré return map $\hat{F}_1 : D_1^{sl} \to D$ as a composition $\hat{F}_1 = T_4 T_3 \hat{T}_2 T_1$ of maps

$$\begin{aligned} &T_1 : D_1^{sl} \to S_1, \\ &\hat{T}_2 : S_1 \to S_2^+, \\ &T_3 : S_2^+ \to l^+, \\ &T_4 : l^+ \to D. \end{aligned} \tag{14}$$

Thus, map $\hat{F}_1$ transfers the points from D_1^{sl} to vertical half-plane S_1 by the trajectories of saddle system A_s (this part is identical to the action of map F_1). Then, the points are mapped by $\hat{T}_2$ to stable sliding half-plane S_2^+ by the trajectories of focus system A_r. The subsequent action of map T_3 transfers these points along S_2^+ down to its border l^+ by the trajectories of Filippov system (8). Finally, these points reach cross section D by the action of map T_4, governed by the trajectories of focus system A_r. Figures 2(a) and 2(b) illustrate this transition and the action of map $\hat{F}_1$.

Note that the part of cross section $D_1 \setminus D_1^{sl}$ corresponds to the set of initial conditions for the trajectories that cannot reach stable sliding half-plane S_2^+. Therefore, the original map (12) is applicable to this part of the cross section.

In the following, we will establish an analytical form of Poincaré return map $\hat{F}_1$. This will also allow us to obtain its odd-symmetrical complement map $\hat{F}_2 : D_2^{sl} \to D$. Readers who are willing to accept the derivation of the Poincaré return map without proof can proceed to Subsection III C without loss of continuity.

B. The analytical derivation

Similarly to the derivation of map (12) with no sliding motions,[7] we obtain the analytical form of map $\hat{F}_1 = T_4 T_3 \hat{T}_2 T_1$ by solving a boundary value problem for each map composing $\hat{F}_1$.

1. Map $T_1 : D_1^{sl} \to S_1$

We begin with a point with initial conditions $x(0), y(0), z(0) = b$ on cross section D_1^{sl}. This point is transferred by a trajectory of saddle system A_s to a point with coordinates $(x(\tau) = 1, y(\tau), z(\tau))$ on half-plane section S_1 in time τ_1. Therefore, using the solution (3) of system A_s with the above initial and final boundary conditions, we obtain the transition time τ_1 and coordinates $y(\tau), z(\tau)$,

$$\begin{aligned} \tau_1 &= -\ln x(0), \\ y(\tau_1) &= y(0)\, e^{-\alpha\tau_1}, \\ z(\tau_1) &= b\, e^{-\nu\tau_1}. \end{aligned} \tag{15}$$

Substituting τ_1 into the y and z equations yields the explicit form of map T_1,

$$T_1 : \begin{aligned} y(\tau_1) &= y(0)\, e^{\alpha \ln x(0)} = y(0) x^{\alpha}(0), \\ z(\tau_1) &= b\, e^{\nu \ln x(0)} = b x^{\nu}(0). \end{aligned} \tag{16}$$

2. Map $\hat{T}_2 : S_1 \to S_2^+$

Map $\hat{T}_2$ further transfers point $[1, y(\tau_1), z(\tau_1)]$ to the stable sliding half-plane S_2^+ in time τ_2 by a trajectory of focus system A_r. This transition time can be implicitly calculated from the final boundary condition, $x(\tau_2) = -1$, on S_2^+, where x is taken from solutions (4). This boundary condition takes the form

$$[b - z(\tau_1)]\, e^{-\lambda\tau_2} \sin(\omega\tau_2) + 2 = 0. \tag{17}$$

However, we choose not to use this implicit form of τ_2 as we will be able to reduce implicitly defined 2D Poincaré return map $\hat{F}_1$ for iterates of x and y coordinates to a 1D explicit x variable map that is sufficient to fully characterize the bifurcations and dynamics in the study. Thus, substituting $(1, y(\tau_1), z(\tau_1))$ and τ_2 into (4), we obtain map $\hat{T}_2$,

$$\begin{aligned} x(\tau_2) &= -1, \\ y(\tau_2) &= 1 + [y(\tau_1) - 1] e^{-\delta\tau_2}, \\ z(\tau_2) &= b - [b - z(\tau_1)] e^{-\lambda\tau_2} \cos(\omega\tau_2), \end{aligned} \tag{18}$$

where $\tau_2 \in \left(\dfrac{\pi}{\omega}, \dfrac{3\pi}{2\omega}\right)$. These lower and upper bounds, π/ω and $3\pi/\omega$, come from the condition $\cos\omega\tau^* = 0$ obtained by setting $z(\tau^*) = b$ in the z-equation of (4) where τ^* corresponds to the times it takes the focus trajectory to intersect the level $z = b$ of cross section D. The lower bound $\tau_{fst}^* = \pi/\omega$ corresponds to the first intersection on the uprising part of the trajectory on the way to S_2^+ [see the blue line in Figs. 2(a) and 2(b)]. The upper bound $\tau_{scn}^* = 3\pi/\omega$ would correspond to the second intersection on the downward part of the trajectory; however, the trajectory hits S_2^+ earlier, thereby placing τ_2 between the two bounds.

3. Map $T_3 : S_2^+ \to l^+$

The most challenging piece in the derivation of complete map $\hat{F}_1$ is the construction of T_3 that describes how points are transferred by trajectories of 2D Filippov sliding system (8) on stable sliding surface S_2^+. While the z-equation in system (8) is uncoupled and integrable, solutions $[y(t), z(t)]$ can only be written in an implicit form. We choose a more efficient approach to building map T_3 by analyzing the relative dynamics of dy/dz in system (8). Toward our ultimate goal of constructing the 1D explicit x variable map, we will show that the y direction along sliding half-plane S_2^+ is contracting so that the y coordinate decreases under the action of T_3. As a result, we will prove that the sliding dynamics along the y direction is always stable.

Recall that $\dot{z} < 0$ at S_2^+ and z always decreases along S_2^+. The y nullcline $\dot{y} = 0$ of sliding system (8) is the hyperbola $y = \dfrac{a}{z - b - a}$ that intersects the border l^+ at the point $(z = b^+, y = 1)$ (Fig. 3). As a result, the vector field of system (8) at the borders $y = 0$, $y = 1$ of sliding surface S_2^+ is oriented inside of S_2^+ since $\dot{y}|_{y=0} > 0$ and $\dot{y}|_{y=1} < 0$. Therefore, the trajectories of system (8) with initial conditions at each level line

$$l^{sl} = \left[z = z^*, y \in (0, 1)\right] \tag{19}$$

reach the line segment l^+, generating map T_3.

To quantify these properties and define map T_3, we introduce a linear nonhomogeneous equation for dy/dz, obtained by dividing

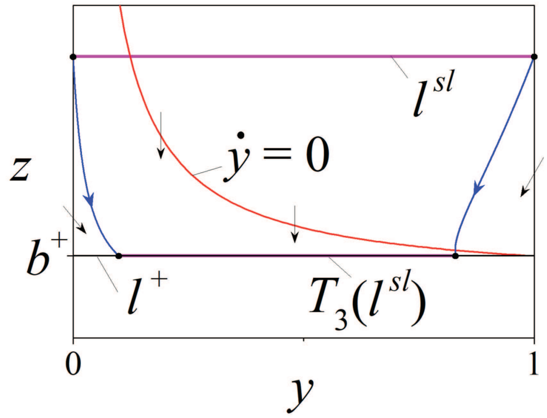

FIG. 3. The vector field of sliding system (8) on half-plane S_2. The vector field in the z direction always points down. The vector field in the y direction below (above) the y nullcline $\dot{y} = 0$ is oriented to the right (left), shrinking image $T_3(l^{sl})$ (purple) of sliding level line l^{sl} (pink).

the first equation in (8) by the second one,

$$\frac{dy}{dz} = P(z)y + Q(z), \tag{20}$$

where

$$P(z) = \frac{\delta}{\omega\left(1 + a(z-b) + \dfrac{a}{z-b-a}\right)} > 0,$$

$$Q(z) = \frac{\delta a}{-\omega(z-b-a)\left(1 + a(z-b) + \dfrac{a}{z-b-a}\right)} < 0.$$

The general solution of linear equation (20) has the form

$$y(z) = c_0 \exp \int_{b^+}^{z^*} P(z)dz + y_p(z), \tag{21}$$

where c_0 is a constant and $y_p(z)$ is a particular solution.

Using the initial condition $y = y(b^+)$, we obtain the constant $c_0 = y(b^+) - y_p(b^+)$. Applying the boundary condition $y = y(z^*)$ with $z^* > b^+$ being the constant defining line l^{sl}, we obtain the equation

$$y(b^+) = y_p(b^+) + h\left[y(z^*) - y_p(z^*)\right], \tag{22}$$

where $h = \exp\left(-\int_{b^+}^{z^*} P(z)dz\right) < 1$ since $P(z) > 0$ for $z > b^+$ and $z^* > b^+$. Equation (22) determines the mapping of a point on any level line l^{sl} with coordinates $\{x = -1, y(z^*), z^*\}$ to a point with coordinates $\{x = -1, y(b^+), b^+\}$ on the lower border of S_2^+, line l^+. Therefore, introducing the notations $y = y(z^*)$ for the initial point's coordinate, $\bar{y} = y(b^+)$ for its image on l^+, and $c = y_p(b^+) - hy_p(z^*)$ for the constant quantity, we can turn Eq. (22) into the contracting linear map $T_3 : S_2^+ \to l^+$,

$$\bar{y} = hy + c. \tag{23}$$

Note that in the limiting case where $z^* \to b^+$ and the size of the relevant sliding region shrinks to zero, constants $c \to 0$ and $h \to 1$ and make T_3 the identity map.

Having reached line l^+, the trajectories of system (1) leave stable sliding half-plane S_2^+ and finally return to cross section D. Therefore, it remains to derive map $T_4 : l^+ \to D$ to complete the composition of $\hat{F}$.

4. Map T_4: $l^+ \to D$

Map T_4 transfers a point $[x = -1, y = y(\tau_3), z = b^+]$ at l^+ along a trajectory of focus system A_r to a point on cross section D with $z = b$ in time τ_4. Therefore, similarly to the construction of map $\hat{T}_2$, we solve the boundary value problem for system A_r to calculate the transition time τ_4 and obtain explicit solutions for $x(\tau_4)$ and $y(\tau_4)$. The general solution of homogeneous linear system A_r (1) subject to some initial conditions x_0, y_0, z_0 can be written in the form

$$\begin{aligned} x(t) &= 1 + \sqrt{(x_0-1)^2 + (z_0-b)^2}\, e^{-\lambda t} \cos(\omega t + \varphi_0), \\ y(t) &= 1 + (y_0 - 1)\, e^{-\delta t}, \\ z(t) &= b + \sqrt{(x_0-1)^2 + (z_0-b)^2}\, e^{-\lambda t} \sin(\omega t + \varphi_0), \end{aligned} \tag{24}$$

where phase shift $\varphi_0 = \arctan \frac{z_0 - b}{x_0 - 1} + n\pi$, $n = 0, 1, \ldots$. Substituting the initial conditions $x_0 = -1$, $y_0 = y(\tau_3)$, $z_0 = b^+ \equiv b + 2\lambda/\omega$ at line l^+ and the boundary condition $z(\tau_4) = b$ at D into (24) and setting $t = \tau_4$, we obtain

$$\begin{aligned} x(\tau_4) &= 1 + 2\sqrt{1 + \lambda^2/\omega^2}\, e^{-\lambda\tau_4} \cos\left(\omega\tau_4 - \arctan\frac{\lambda}{\omega} + \pi\right), \\ y(\tau_4) &= 1 + (y(\tau_3) - 1)\, e^{-\delta t}, \\ b &= b + 2\sqrt{1 + \lambda^2/\omega^2}\, e^{-\lambda\tau_4} \sin\left(\omega\tau_4 - \arctan\frac{\lambda}{\omega} + \pi\right). \end{aligned} \tag{25}$$

From the last equation in (25), we get the condition $\sin(\omega\tau_4 - \arctan\frac{\lambda}{\omega}) = 0$, which yields transition time $\tau_4 = \frac{1}{\omega} \arctan \frac{\lambda}{\omega}$. Therefore, system (25) yields explicit map T_4,

$$T_4 : \begin{aligned} x(\tau_4) &= 1 - \gamma_{cr}, \\ y(\tau_4) &= 1 + (y(\tau_3) - 1)\, e^{-\frac{\delta}{\omega} \arctan \frac{\lambda}{\omega}}, \\ z(\tau_4) &= b, \end{aligned} \tag{26}$$

where

$$\gamma_{cr} = 2\sqrt{1 + \lambda^2/\omega^2}\, e^{-\frac{\lambda}{\omega} \arctan \frac{\lambda}{\omega}} = b_{cr}\, e^{-\frac{3\pi\lambda}{2\omega}} \tag{27}$$

with b_{cr} as in no-sliding condition (10).

Before assembling final map $\hat{F}_1 = T_4 T_3 \hat{T}_2 T_1 : D_1^{sl} \to D$, we need to explicitly determine the size of cross section D_1^{sl} that corresponds to trajectories that start from D_1 and reach stable sliding half-plane S_2^+.

5. Region D_1^{sl} of initial conditions for sliding trajectories

To find the border of region D_1^{sl}, we need to find the pre-image of line l^+ under the action of composition map $\hat{T}_2 T_1$. In fact, any trajectory starting from this border on cross section D eventually falls onto line l^+ [the blue trajectory in Fig. 2(a) is a case in point]. Therefore, we can specify the equations of map $\hat{T}_2$ (18) to such a trajectory with $z(\tau_2') = b^+$, where τ_2' is time τ_2 specific to this trajectory. Thus, from (5)–(18), we obtain

$$\begin{aligned} x(\tau_2) &= -1 = 1 + [b - z(\tau_1)]\, e^{-\lambda \tau_2'} \sin(\omega \tau_2'),\\ y(\tau_2) &= 1 + [y(\tau_1) - 1]\, e^{-\delta \tau_2},\\ z(\tau_2) &= b - [b - z(\tau_1)]\, e^{-\lambda \tau_2} \cos(\omega \tau_2). \end{aligned} \tag{28}$$

Substituting the initial condition $z(\tau_1)$ (16) into (28) and replacing $b^+ = b + 2\lambda/\omega$, we transform its x and z equations into the form

$$\begin{aligned} -2 &= [b - bx^{\nu}(0)]\, e^{-\lambda \tau_2'} \sin(\omega \tau_2'),\\ -2\lambda/\omega &= [b - bx^{\nu}(0)]\, e^{-\lambda \tau_2'} \cos(\omega \tau_2'). \end{aligned} \tag{29}$$

Dividing the first equation by the second equation and solving for τ_2', we obtain the transition time

$$\tau_2' = \frac{1}{\omega}\left(\arctan \frac{\omega}{\lambda} + \pi\right). \tag{30}$$

Substituting τ_2' back into the first equation and solving for $x(0)$ using a trigonometric identity, we finally derive the equation for the pre-image of line l^+, the border of region D_1^{sl},

$$x_s = \left(1 - \frac{2\sqrt{1+\lambda^2/\omega^2}}{b}\, e^{\frac{1}{\omega}\left(\arctan \frac{\omega}{\lambda} + \pi\right)}\right)^{\frac{1}{\nu}} = \left(1 - \frac{\gamma_{cr}}{\gamma}\right)^{\frac{1}{\nu}}. \tag{31}$$

Therefore, $D_1^{sl} = (x \le x_s, y \le 1, z = b)$. Due to the piecewise-system's odd symmetry $(x, y, z) \to (-x, -y, z)$, the entire region $D^{sl} = D_1^{sl} \bigcup D_2^{sl}$ is defined as follows:

$$D_{sl} = (|x| \le x_s, |y| \le 1, z = b). \tag{32}$$

6. Final map $\hat{F}$: putting pieces together

To derive the final form of $\hat{F}_1 : T_4 T_3 \hat{T}_2 T_1$, we combine the equations for maps T_1 (16), $\hat{T}_2$ (18), T_3 (23), and T_4 and obtain

$$\hat{F}_1 : \begin{array}{l} \bar{x} = 1 - \gamma_{cr},\\ \bar{y} = r_1(x) + R_1(x) y, \end{array} \qquad \text{for } (x, y) \in D_1^{sl}, \tag{33}$$

where

$$\begin{aligned} r_1(x) &= 1 + (c - 1 + h(1 - e^{-\delta\tau_2}))\, e^{-\frac{\delta}{\omega} \arctan \frac{\lambda}{\omega}},\\ R_1(x) &= h x^{\alpha}\, e^{-\delta\tau_2 - \frac{\delta}{\omega} \arctan \frac{\lambda}{\omega}}. \end{aligned} \tag{34}$$

Here, constants c and h are implicit functions of x through the dependence $z^+ = z(\tau_2)$ in map $\hat{T}_2$. Constant τ_2 can be calculated from (17) with $z(\tau_1)$ from (16). As in (12), $\bar{x}$ and $\bar{y}$ are the images of x and y, respectively.

Due to the odd symmetry in x and y, it is straightforward to derive the complement map $\hat{F}_2 : D_2^{sl} \to D$ from (33) by replacing $(\bar{x}, \bar{y})$ and (x, y) with $-(\bar{x}, -\bar{y})$ and $(-x, -y)$, respectively. This change will not explicitly affect function $r_1(x)$ as it is an implicit function of x.

Thus, combining $\hat{F}_1$ and $\hat{F}_2$, we finally derive the Poincaré return map $\hat{F} : D^{sl} \to D$ as follows:

$$\hat{F} : \begin{array}{l} \bar{x} = (1 - \gamma_{cr}) \operatorname{sign} x,\\ \bar{y} = r_1(x) + R(x) y, \end{array} \qquad \text{for } (x, y) \in D_{sl}, \tag{35}$$

where $R(x) = h|x|^{\alpha}\, e^{-\delta\tau_2 - \frac{\delta}{\omega} \arctan \frac{\lambda}{\omega}} < 1$.

C. The complete 2D map

Having derived Poincaré return map $\hat{F}$ (35) that describes the dynamics of the attractor's trajectories that contain pieces of sliding motions, we can finally modify map $F : D \to D$ (12) to incorporate sliding motions. This is done by combining map $\hat{F}$ defined for D_{sl} with map F (12) defined for $D \setminus D_{sl}$. Thus, with the abuse of notation, this new complete 2D map F becomes

$$\begin{aligned} \bar{x} &= \begin{cases} (1 - \gamma_{cr}) \operatorname{sign} x & \text{for } |x|^{\nu} \le \frac{\gamma - \gamma_{cr}}{\gamma},\\ (1 - \gamma + \gamma |x|^{\nu}) \operatorname{sign} x & \text{for } |x|^{\nu} > \frac{\gamma - \gamma_{cr}}{\gamma}, \end{cases}\\ \bar{y} &= \begin{cases} r_1(x) + R(x) y & \text{for } |x|^{\nu} \le \frac{\gamma - \gamma_{cr}}{\gamma},\\ (1 - r) \operatorname{sign} x - r|x|^{\alpha} y, & \text{for } |x|^{\nu} > \frac{\gamma - \gamma_{cr}}{\gamma}, \end{cases} \end{aligned} \tag{36}$$

where $|x| = x_s = \left(\frac{\gamma - \gamma_{cr}}{\gamma}\right)^{\frac{1}{\nu}}$ determines the border of D_{sl} with parameter γ_{cr} defined in (27).

Similar to its original counterpart (12), this map has a triangular form such that its x equation does not depend on y and drives the y equation. This triangular form originates from our choice of the linear systems composing the piecewise-smooth system (1), which uncouple the x and z variables from the y variable in focus systems A_l and A_r. Therefore, the motions in the x and z directions are independent from the motion along the y axis. As in Ref. 7, we call the 1D x map the *master* map and use its properties to characterize the dynamics and bifurcations in piecewise-smooth system (1).

A remarkable property of the driven y equation of map (36) is its simple converging dynamics that indicates that the y direction in piecewise-smooth system (1) is stable. This property for the sliding component of the map is determined by contracting factor $R(x) < 1$ and by contraction guaranteed by the $r|x|^{\alpha} < 1$ factor for the non-sliding component of the map (see Ref. 7 for the details). Thus, we can extend the claim of Lemma 2 in Ref. 7 to map (36) and state that any stable (unstable) p-periodic orbit of the 1D master x map induces a stable (saddle) p-periodic orbit in the full 2D map (36). Therefore, attractors of piecewise-smooth system (1) and their bifurcations can be fully characterized by the 1D master map.

D. 1D master map: The standard form

Obtained from 2D map (36) by removing the driven y equation, 1D master map $\bar{x} = f(x)$ explicit in the parameters of system (1) reads

$$\begin{aligned} \bar{x} &= (1-\gamma_{cr})\operatorname{sign} x && \text{for } |x|^{\nu} \le \frac{\gamma-\gamma_{cr}}{\gamma}, \\ \bar{x} &= (1-\gamma+\gamma|x|^{\nu})\operatorname{sign} x && \text{for } |x|^{\nu} > \frac{\gamma-\gamma_{cr}}{\gamma}. \end{aligned} \tag{37}$$

Originated from (36), the master map is also discontinuous at point $x = 0$ that corresponds to two symmetrical homoclinic orbits to saddle O_s in piecewise-smooth system (1) with parameters satisfying the condition $\gamma = \gamma_{cr} = 1$. Similarly, the master map (37) has two fixed points $e_l = x_1^* = -1$ and $e_r = x_2^* = 1$ at the ends of the interval $X \in [-1, 1]$ that correspond to equilibrium points e_l and e_r of piecewise-smooth system (1).

For convenience, 1D map master (37) can be turned into a variation of the standard 1D Lorenz map,[1,2,45,63,64]

$$\bar{\xi} = g(\xi) \equiv \begin{cases} (-\mu+\varepsilon)\operatorname{sign}\xi & \text{for } |\xi|^{\nu} \le \varepsilon, \\ (-\mu+|\xi|^{\nu})\operatorname{sign}\xi & \text{for } |\xi|^{\nu} > \varepsilon \end{cases} \tag{38}$$

by rescaling variable $\xi = kx$ with $k = \gamma^{\frac{1}{\nu-1}}$ and introducing new parameters

$$\begin{aligned} \mu &= (\gamma-1)\gamma^{\frac{1}{\nu-1}}, \\ \varepsilon &= (\gamma-\gamma_{cr})\gamma^{\frac{1}{\nu-1}}. \end{aligned} \tag{39}$$

The use of this standard form of the 1D master map will simplify the analysis and will help elucidate the role of sliding motions in the bifurcation set of map (38) and, ultimately, of piecewise-smooth system (1). Note that the first equation in (38) corresponds to the sliding part of the trajectories in system (1), and the parameter ε determines the size of the corresponding flat fragment in the graph of function $g(\xi)$ via $|\xi| \le \varepsilon^{\frac{1}{\nu}}$. At the same time, the condition $-\mu + \varepsilon = 0$ corresponds to a homoclinic bifurcation of saddle O_s in (1). The corresponding homoclinic orbits contain a portion of sliding motions for $\varepsilon > 0$ and become the classical homoclinic butterfly in the absence of sliding motions for $\varepsilon = 0$. The meaning of parameter μ for trajectories without sliding motions is similar to that of the standard Lorenz map,[45] with an important caveat that this parameter is a function of parameters γ and ν, which has its maximum value at $\gamma = 1/\nu$. Therefore, in contrast to the standard Lorenz map, it cannot be increased any further to make fixed points e_r and e_l disappear via saddle-node bifurcations (see Ref. 7 for the details).

IV. HOMOCLINIC BIFURCATIONS

Armed with analytically tractable master map (38), we can now proceed with a rigorous description of discontinuity-induced homoclinic bifurcations in piecewise-smooth system (1). We begin with a non-smooth analog of the classical homoclinic butterfly bifurcation in the absence of sliding motions. We then prove that the appearance of any small piece of sliding motions in the otherwise unstable homoclinic butterfly can generate a stable periodic orbit.

A. The classical homoclinic butterfly bifurcation: The birth of saddle cycles

This homoclinic bifurcation in piecewise-smooth system (1) was described in our previous paper.[7] Here, we briefly review the statement of Theorem 2 in Ref. 7 to convince the reader that the homoclinic butterfly orbit in the absence of sliding motions is unstable, as in the original smooth Lorenz system. To make the direct connection to the master map (38), we shall formulate a partial statement of Theorem 2[7] in terms of parameters μ and ε that can be directly turned into the parameters of map (37) and of the original flow system (1).

Consider piecewise-smooth system (1) in parameter range (10) that guarantees that its attractors do not contain sliding motions. In terms of the master map (38), this amounts to the condition $\varepsilon < 0$; therefore, the inequality in the first equation of (38) cannot be satisfied, and (38) becomes the standard Lorenz map with the caveat mentioned above. Thus, Theorem 2 in Ref. 7 guarantees the following.

1. For $\mu < 0,\ \varepsilon < 0:$ the master map (38) has two stable fixed points $e_r(\xi = k)$ and $e_l(\xi = -k)$ whose basins of attraction are the entire interval $(-k, k)\backslash(\xi = 0)$. In terms of piecewise-smooth system (1), this implies that two stable foci e_l and e_r attract all system's trajectories except for saddle O_s and its stable 2D manifold [Fig. 4(a)].
2. For $\mu = 0,\ \varepsilon < 0:$ the singular point $\xi = 0$ maps into itself yielding the homoclinic butterfly of saddle O_s [Fig. 4(b)].
3. For $\varepsilon < 0:$ increasing μ from $\mu = 0$ induces (i) two unstable points $p_r^u(\xi = \xi_r)$ and $p_l^u(\xi = \xi_l = -\xi_r)$ that correspond to two saddle limit cycles [dashed orbits in Fig. 4(c)] and (ii) a nontrivial hyperbolic Cantor set of unstable trajectories.

This bifurcation transition is depicted in Figs. 6(a) and 6(b) in Ref. 7 for the master map (37) and, therefore, is not shown in this paper. Notice that this transition is a direct non-smooth analog of the classical homoclinic butterfly bifurcation in the original smooth Lorenz system.

B. Non-classical sliding homoclinic bifurcations

In this subsection, we present one of the main results of this paper, which demonstrates that homoclinic bifurcations in the presence of sliding motions can result in dynamics that are drastically different from their smooth analogs.

We begin with the same setting used in Subsection IV A where piecewise-smooth system (1) has saddle O_s and two stable foci in the absence of sliding motions. The following theorem describes what happens to the system's dynamics when the homoclinic butterfly becomes tangent to the stable sliding plane and, therefore, contains a small portion of sliding motions. For clarity, we first formulate the claims in terms of parameters and dynamics of master map (38) and relate them to the flow of piecewise-smooth system (1).

Theorem 1 (unstable homoclinic orbits generate a stable cycle)**.**

1. *Before the bifurcation. For $\mu < 0, \varepsilon < 0:$ two stable fixed points $e_r(\xi = k)$ and $e_l(\xi = -k)$ are the only attractors of the master map* (38)*. The piecewise-smooth system* (1) *has two stable foci e_l and e_r and saddle O_s [Figs. 5(a), 5(d), and 5(g)].*
2. *The homoclinic bifurcation with sliding tangency. For $\mu = 0,\ \varepsilon = 0:$ the singular point $\xi = 0$ maps into itself and generates two unstable homoclinic orbits of saddle O_s in piecewise-smooth system* (1) *[Figs. 5(b), 5(e), and 5(h)]. Each of*

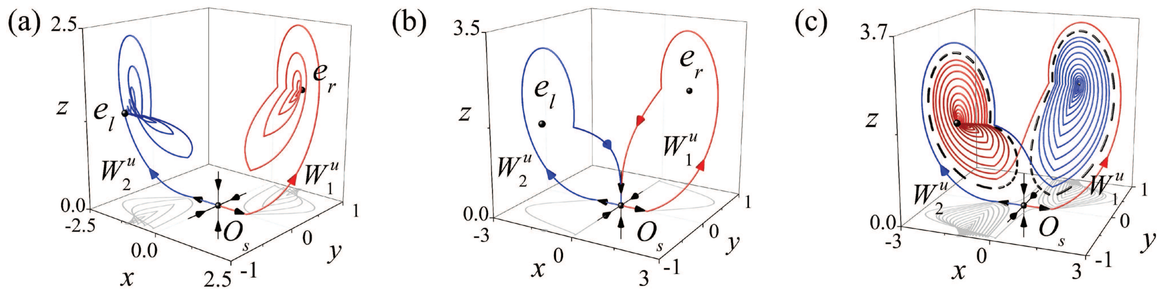

FIG. 4. The classical homoclinic butterfly bifurcation in piecewise-smooth system (1) under no-sliding condition (10). (a) The phase portrait at $b = 1.5 < b_h = \exp\{3\pi\lambda/(2\omega)\}$ [$\mu = -0.569$, $\varepsilon = -2.795$ in master map (38)] before the bifurcation. Two stable foci e_l and e_r (black circles) attract the unstable manifolds (red and blue) of saddle O_s. (b) The phase portrait at $b = b_h = 2$ ($\mu = 0$, $\varepsilon = -0.979$) at the homoclinic bifurcation. The unstable manifolds (red and blue) of saddle O_s form the homoclinic butterfly. The piecewise-smooth shape of the homoclinic orbit is due to the non-smooth nature of (1). (c) The phase portrait at $b = 2.02 > b_h$ ($\mu = 0.01$, $\varepsilon = -0.942$) after the bifurcation. Two saddle cycles (dashed), co-existing with stable foci, were born as a result of the homoclinic bifurcation. Other parameters are $\lambda = 0.1471$, $\omega = 1$, $\lambda = a$, $\nu = 0.65$, $\alpha = 2$, $\delta = 0.588$.

the homoclinic orbits is tangent to one of the sliding half-planes S_1^+ *and* S_2^+.

3. *After the bifurcation. For* $\varepsilon > 0$: *increasing* $\mu \in (\varepsilon, \varepsilon + \varepsilon^{1/\nu})$ *generates a period-2 stable fixed point* $p^s_{l,r}$ *and two unstable fixed points* $p^u_r(\xi = \xi_r)$ *and* $p^u_l(\xi = \xi_l = -\xi_r)$ *in master map (38). Therefore, piecewise-smooth system (1) has a stable period-2 limit cycle and two saddle limit cycles that were born simultaneously from the homoclinic orbit [Figs. 5(c), 5(f), and 5(i)]. In contrast to the classical homoclinic butterfly bifurcation, the master map (38) does not contain a hyperbolic Cantor set of unstable trajectories due to the presence of sliding motions.*

Proof. Claim 1 is identical to Claim 1 in the formulation of the classical homoclinic bifurcation in piecewise-smooth system (1) in the absence of sliding and is guaranteed by Theorem 2 in Ref. 7.

The formation of the homoclinic orbit at $\mu = 0$, $\varepsilon = 0$ in Claim 2 is guaranteed by the structural properties of piecewise-smooth system (1) so that the singular fixed point $\xi = 0$ in master map (38) maps line $l = W^s \cap D : x = 0$ on cross section D in piecewise-smooth system (1) into saddle O_s. By continuation, the saddle point is mapped back into line $l : x = 0$, forming the homoclinic orbit. The emergence of the singular fixed point $\xi = 0$ at $\mu = 0$, $\varepsilon = 0$ follows from the right-hand sides of master map (38) that become equal to zero at $\mu = 0$, $\varepsilon = 0$.

The emergence of stable period-2 fixed point $p^s_{l,r}$ for $\varepsilon > 0$ when $\varepsilon < \mu < \varepsilon + \varepsilon^{1/\nu}$ in Claim 3 is guaranteed by the appearance of two symmetrical horizontal fragments of length $\xi = \varepsilon^{1/\nu}$ in the graph of function $g(\xi)$ that yield intersections with line $\bar{\xi} = -\xi$ [Fig. 5(c)]. These intersections correspond to symmetrical points $p^s_r(\xi = \mu - \varepsilon, \bar{\xi} = \varepsilon - \mu)$ and $p^s_l(\xi = \varepsilon - \mu, \bar{\xi} = \mu - \varepsilon)$, which form stable period-2 point $p^s_{l,r}$. Its stability is guaranteed by the zero derivative $g'(\xi)$ at $p^s_{l,r}$ in the region $0 < \varepsilon < \mu \leq \varepsilon + \varepsilon^{1/\nu}$. This period-2 point loses its stability when $\mu > \varepsilon + \varepsilon^{1/\nu}$ as the horizontal fragments of the graph do no longer intersect line $\bar{\xi} = -\xi$, whereas the non-flat parts of the graph of $g(\xi) = (-\mu + |\xi|^\nu)\operatorname{sign}\xi$ in (38) preserve period-2 point $p^s_{l,r}$ but make it unstable.

The emergence of two unstable fixed points $p^u_r(\xi = \xi_r)$ and $p^u_l(\xi = \xi_l = -\xi_r)$ after the homoclinic bifurcation is guaranteed since the equation $\mu = \xi^\nu - \xi$ that determines the existence of fixed points for $\xi > 0$ has two solutions in the considered region of μ. The larger solution yields the coordinate of stable point e_r that is preserved by the homoclinic bifurcation and the smaller solution corresponds to ξ_r. The instability of $p^u_r(\xi = \xi_r)$ and $p^u_l(\xi = \xi_l = -\xi_r)$ is guaranteed by $|g'(\xi)| > 1$ at $\xi = -\xi_r, \xi_r$.

In the classical homoclinic butterfly case of Fig. 4(c) in the absence of sliding ($\varepsilon < 0$), the master map (38) has two intervals of ξ on which a Cantor set of unstable trajectories is lying (see Ref. 7 for details). The appearance of the two horizontal fragments in the graph of function $g(\xi)$ due to sliding motions for $\varepsilon > 0$ in Claim 3 makes the two intervals of ξ collapse into symmetrical points p^s_r and p^s_l. As discussed above, these points form a super-stable period-2 point $p^s_{l,r}$. Therefore, the hyperbolic Cantor set of unstable trajectories may not exist for $\varepsilon < \mu < \varepsilon + \varepsilon^{1/\nu}$. ☐

Remark 1. Note that saddle value $\eta = 1 - \nu$ of saddle O_s is positive, and the homoclinic orbit formed at $\mu = 0$ and $\varepsilon = 0$ is unstable as it repels trajectories [see the typical trajectory (the blue spiral) in Fig. 5(d) that diverges from the homoclinic orbit and approaches stable fixed point e_r].

Remark 2. Claim 3 of Theorem 1 is applicable to any small value of $\varepsilon > 0$; therefore, the emergence of an arbitrarily small portion of sliding motions in the unstable homoclinic orbit induces stable dynamics in the form of the stable period-2 cycle.

Remark 3. Further increasing μ beyond the interval $\mu \in (\varepsilon, \varepsilon + \varepsilon^{1/\nu})$ such that $\mu - \varepsilon > \xi_r$ leads to the emergence of a hyperbolic Cantor set of unstable trajectories. This Cantor set is present as long as the unstable fixed point $p^u_r(\xi = \xi_r)$ exists. In terms of Fig. 5(c), this condition implies that the horizontal fragment with coordinate $\xi = \mu - \varepsilon$ lies above the unstable point p^u_r. The emergence and disappearance of such Cantor sets of unstable trajectories in the higher order kth-iterate maps $g^k(\xi)$ may be the origin of the chaotic windows in Fig. 8.

Figure 5 illustrates the bifurcation transition guaranteed by Theorem 1 and achieved by varying only one parameter λ in piecewise-smooth system (1). Although the conditions of Theorem 1 are conveniently formulated in terms of parameters μ and ε of master map (38), we chose to plot the diagrams in the top row of Fig. 5 for master map (37) as its fixed points $e_l(x = -1)$ and $e_r(x = 1)$

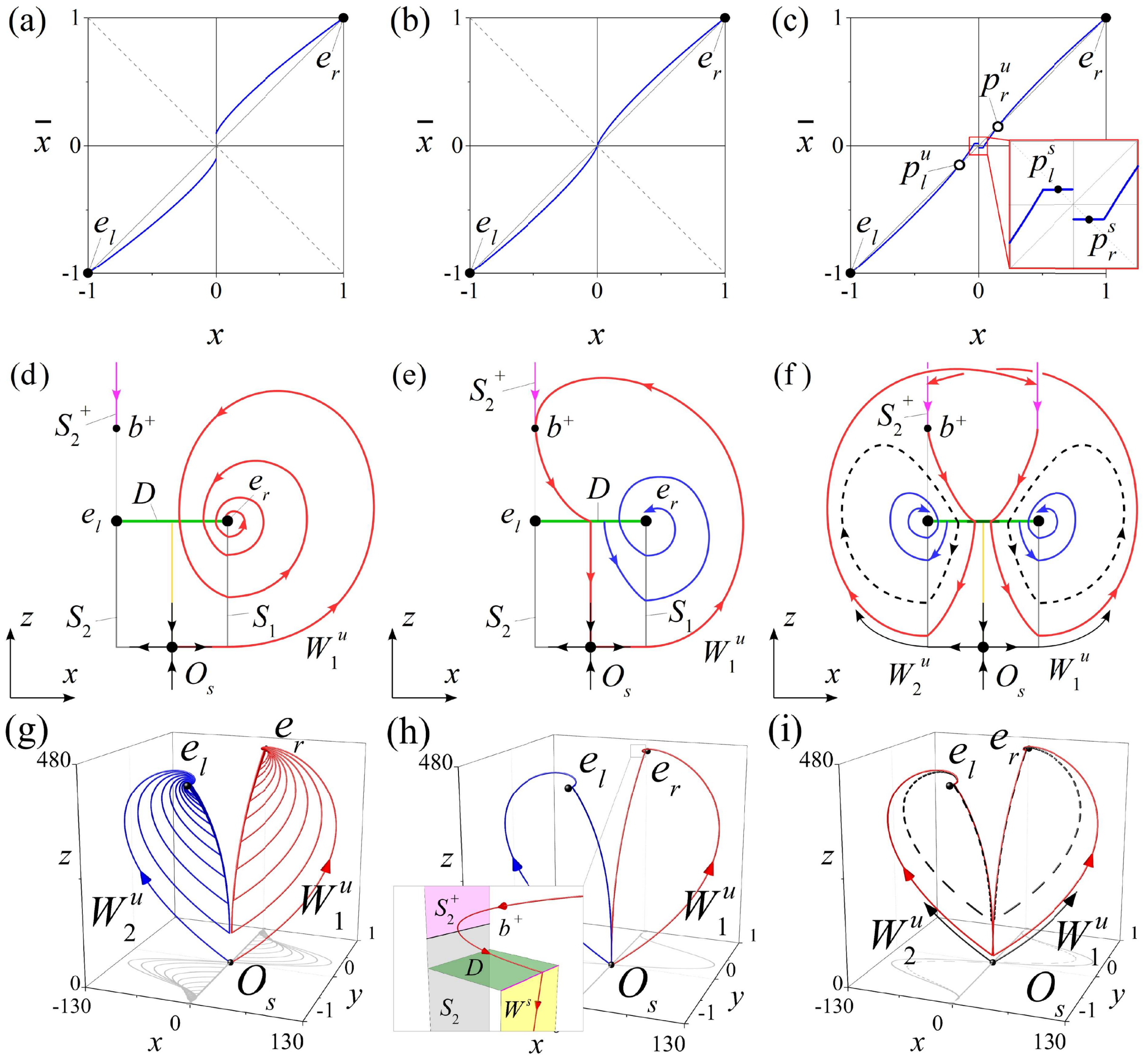

FIG. 5. The non-classical sliding homoclinic bifurcation (illustration of Theorem 1). Top row: Bifurcation transition in master map (37) as a function of parameter ε and μ [their correspondence to γ and γ_{cr} is given in (39)]. (a) Before the bifurcation: $\mu = -0.164$, $\varepsilon = -0.131$. Two stable fixed points e_l and e_r (solid circles). Disjoint leaves of the graph of $f(x)$ (blue). (b) The bifurcation: $\mu = 0$, $\varepsilon = 0$. The leaves of the graph of $f(x)$ (blue) joint each other to form singularity fixed point $x = 0$. (c) After the bifurcation: $\mu = 0.0582$, $\varepsilon = 0.047$. The emergence of a period-2 stable point formed by points p_l^s and p_r^s (zoomed-in in the inset) and two unstable points p_l^u and p_r^u (open circles). Middle and bottom rows: The corresponding dynamics of piecewise-smooth system (1) as a function of parameter λ that changes μ and ε in the top row accordingly. (d) and (g) Before the bifurcation: $\lambda = 1.32$. Unstable manifold W_1^u (red) cannot reach stable sliding half-plane S_2^+ and is attracted by stable fixed point e_r. (e) and (h) Homoclinic bifurcation with sliding tangency: $\lambda = 1.298\,127$. Unstable manifold W_1^u (red) is tangent to S_2^+ and forms a homoclinic orbit. Blue trajectory in (e) is repelled by the unstable homoclinic orbit and converges toward stable fixed point e_r. Two homoclinic orbits (blue and red) in (h) form a homoclinic butterfly. The inset in (h) details the behavior of unstable manifold W_1^u near sliding half-plane S_2^+ (pink) and cross section D (green). (f) and (i) After the bifurcation: $\lambda = 1.28$. The emergence of stable period-2 orbit (red) with sliding motions [pink in (f)] and two saddle limit cycles (black dashed). Other parameters are $b = 453.629$, $\nu = 0.8$, $\omega = 1$.

bound the graphs of $\bar{x} = f(x)$ to the interval $[-1, 1]$ and provide a more distinctive visual representation of the graph's details for the given set of parameters. The coordinates of fixed points and parameters of maps (37) and (38) are explicitly connected through $\xi = kx$ with $k = \gamma^{\frac{1}{\nu-1}}$ and expressions (39) for μ, ε and γ, γ_{cr}.

Remark 4. The birth of the stable period-2 cycle in the bifurcation transition of Theorem 1 is accompanied by the emergence of two saddle limit cycles that are needed to separate the attraction basins of the stable period-2 limit cycle and stable fixed points e_l and e_r. However, a different bifurcation transition in which sliding

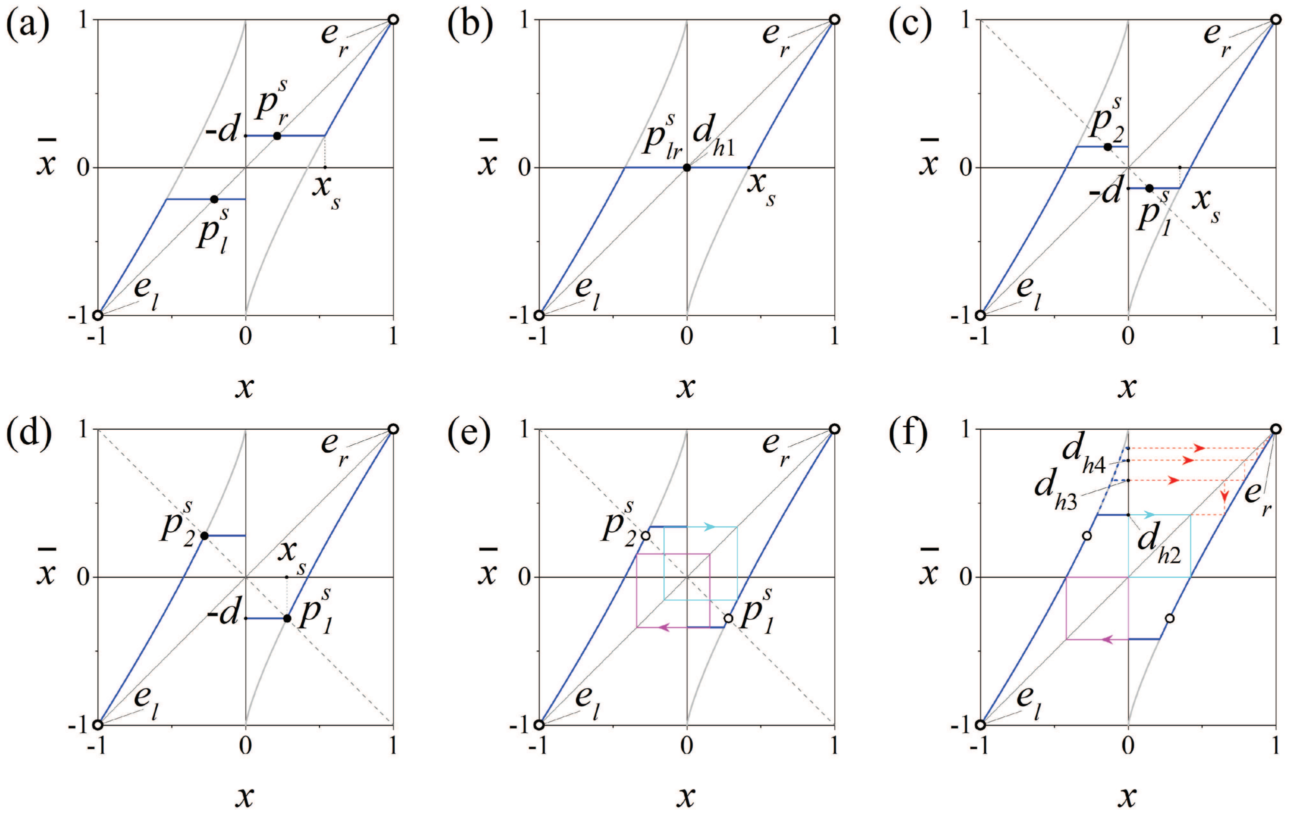

FIG. 6. Graphs of master map (40) (blue line) and the corresponding Lorenz map (43) without sliding (gray line). (a) $d = -0.214$ ($\lambda = 1.55$, $b = 2973.07$). Superstable points $p^s_{l,r}$ (solid circles) attract the entire interval $(-1,1)$. (b) $d = d_{h1} = 0$ ($\lambda = 1.298$, $b = 907.26$). First homoclinic bifurcation. (c) $d = 0.14$ ($\lambda = 1.15$, $b = 451.42$). Stable period-two orbit $p^s_{1,2}$. (d) $d = d_{p1} = 0.279$ ($\lambda = 1.01$, $b = 233.64$). First pitchfork bifurcation of $p^s_{1,2}$. (e) $d = 0.34$ ($\lambda = 0.95$, $b = 175.9$). Two superstable symmetrical period-2 orbits (cyan and magenta) born from the pitchfork bifurcation in (d). (f) $d = d_{h2} = 0.4204$ ($\lambda = 0.8714$, $b = 121.48$). Second homoclinic bifurcation that creates a superstable period-4 orbit by merging the cyan and magenta orbits from (e). The red dashed lines correspond to cobwebbing for subsequent homoclinic bifurcations at $d = d_{h3}$, $d = d_{h4}$, and $d = d_{h5}$ (not labeled). Note the shortening of the horizontal fragments of the graph that induces the accumulation of homoclinic bifurcations when the graph of (40) (blue) approaches its counterpart (43) that displays the strange Lorenz attractor. Other parameters are $\gamma = 2$, $\omega = 1$, $\lambda = a$, $\nu = 0.8$, $\alpha = 2$, $\delta = 0.588$.

motions appear prior to the homoclinic bifurcation can make the homoclinic orbit stable so that it gives birth to a stable period-2 orbit without generating saddle cycles. This is possible when sliding motions appearing before the homoclinic bifurcation first generate two stable and two unstable symmetrical limit cycles due to two symmetrical saddle-node bifurcations at $\mu = \varepsilon - \varepsilon^{1/\nu}$. Further increasing the size of participating sliding motions can lead to a subcritical Andronov–Hopf-like bifurcation when the saddle limit cycles shrink to stable foci e_r, e_l and disappear, rendering e_r, e_l saddle-foci (this transition in the absence of sliding motions is detailed in Ref. 7). Thus, when the homoclinic butterfly is formed around saddle-foci e_r and e_l, it is stable and contains a significant portion of stable sliding motions.

The complete description of all possible complex bifurcation transitions as functions of parameters μ and ε in (38) is beyond the scope of this paper and will be reported elsewhere. Instead, we detail a bifurcation route that involves the formation of stable homoclinic orbits and demonstrate how an infinite sequence of such sliding homoclinic bifurcations leads to the formation of the strange Lorenz-type attractor.

V. A ROUTE TO CHAOS VIA AN INFINITE SEQUENCE OF HOMOCLINIC BIFURCATIONS

First, we seek to characterize a variation of the non-classical sliding homoclinic bifurcation that involves the stable homoclinic orbit mentioned in Remark 4. Second, we aim to derive a scaling factor for sequences of multi-loop homoclinic orbits that is similar to the Feigenbaum constant[65] for cascades of period-doubling bifurcations. Toward these goals, we set parameter $\gamma = 2$ in (37), which limits $\gamma_{cr} \in (0, 2]$. For analytical convenience, we also introduce a bifurcation parameter $d = \gamma_{cr} - 1 \in (-1, 1]$. This particular choice of parameter γ allows one to derive a recurrent formula that gives parameter values for each of the multi-loop homoclinic bifurcations, thereby yielding the explicit scaling factor. Thus, master map (37)

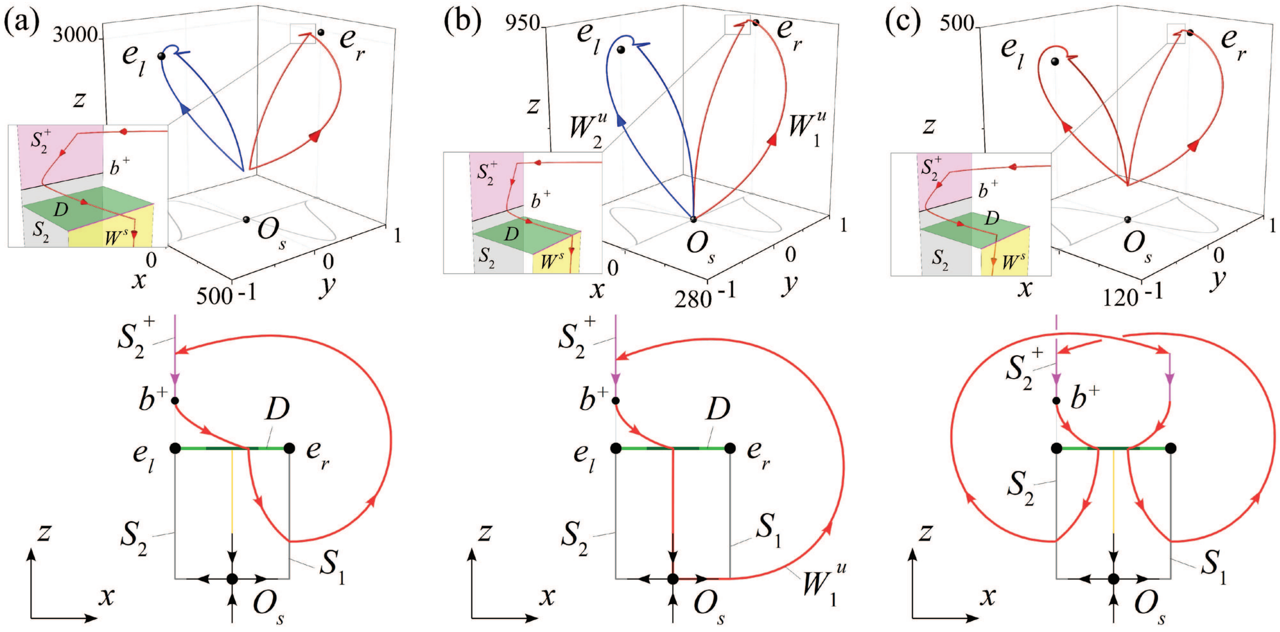

FIG. 7. A variation of the non-classical homoclinic bifurcation: a stable homoclinic butterfly induces a stable period-2 cycle (illustration of Claims 1–3 in Theorem 2). (a) Before the bifurcation: $d = -0.214$. Two stable limit cycles (blue and red lines in the top panel) contain sliding motions (the small pulse-like parts of the trajectories also zoomed-in in the insets). (b) The bifurcation: $d = 0$. The formation of the sliding homoclinic butterfly (top panel). (c) After the bifurcation: $d = -0.14$ stable period-2 limit cycle is the only attractor of system (1) (top panel). The construction of the period-2 limit cycle that contains sliding fragments (pink) (bottom panel). Other parameters are as in Fig. 6. Panels (a), (b), and (c) correspond to panels (a), (b), and (c) in Fig. 6.

becomes

$$\bar{x} = f(x) \equiv \begin{cases} -d\,\mathrm{sign}\, x & \text{for } |x| \le \left(\frac{1-d}{2}\right)^{\frac{1}{\nu}}, \\ (-1+2|x|^{\nu})\,\mathrm{sign}\, x & \text{for } |x| > \left(\frac{1-d}{2}\right)^{\frac{1}{\nu}}. \end{cases} \tag{40}$$

Note that two fixed points $e_l(x=-1)$, $e_r(x=1)$ are unstable since $f'(x)|_{x=\pm 1} = 2\nu > 1$ under condition (6). Therefore, our initial setting differs from that of Theorem 1 as the corresponding fixed points $e_l(x=-1)$, $e_r(x=1)$ in piecewise-smooth system (1) are saddle-foci. As a result, we should expect the formation of stable homoclinic orbits mentioned in Remark 4. The details of this bifurcation transition and a route to chaos in master map (40) as a function of parameter $d \in (-1, 1]$ can be summarized in the following assertion.

Theorem 2 (sliding multi-loop homoclinic bifurcations and a route to chaos)**.**

1. *For $-1 < d < 0$ $(0 < \gamma_{cr} < 1)$, two superstable fixed points $p_l^s(x=d)$ and $p_r^s(x=-d)$ attract all points from the interval (-1,1) except for singularity point $x=0$ [Fig. 6(a)]. Points $p_l^s(x=d)$ and $p_r^s(x=-d)$ correspond to two stable limit cycles in piecewise-smooth system (1) [Fig. 7(a)].*
2. *At $d = d_{h1} = 0$ $(0 < \gamma_{cr} = 1)$, p_l^s and p_r^s merge together at the origin to form a stable homoclinic butterfly in piecewise-smooth system (1) [Figs. 6(b) and 7(b)].*
3. *For $0 < d < d_{p1}$, where d_{p1} is a root of equation $2d^{\nu} + d = 1$, map (40) has superstable period-2 limit cycle $p_{1,2}^s$ [Fig. 6(c)] born from the homoclinic butterfly at $d = d_{h1} = 0$. This limit cycle corresponds to a stable period-2 limit cycle in piecewise-smooth system (1) [Fig. 7(b)].*
4. *At $d = d_{p1}$, the orbit $p_{1,2}^s$ undergoes a supercritical pitchfork bifurcation [Fig. 6(d)]. Increasing $d > d_1$ makes $p_{1,2}^s$ unstable and gives birth to two symmetrical superstable period-2 orbits [cyan and magenta squares in Fig. 6(e)].*
5. *At $d = d_{h2} = \left(\frac{1}{2}\right)^{\frac{1}{\nu}}$, these superstable period-2 orbits merge at the origin and form two symmetrical two-loop homoclinic orbits [Fig. 6(f)].*
6. *For $d_{h2} < d < d_{p2}$, where d_{p2} is a root of equation $2d^{\nu} - \left(\frac{1-d}{2}\right)^{\frac{1}{\nu}} = 1$, map (40) has superstable period-4 limit cycle $p_{1,2}^s$ [Fig. 6(c)] born after the homoclinic bifurcation at $d = d_{h2}$.*
7. *Parameter values for all subsequent multi-loop homoclinic bifurcations are defined by the recursive formula*

$$d_{h(n+1)} = \chi(d_{hn}) = \left(\frac{d_{hn}+1}{2}\right)^{\frac{1}{\nu}}, \tag{41}$$

where $d_{h(n+1)}$ and d_{hn} are the values of parameter d that correspond to homoclinic bifurcations that give birth to $(n+1)$-loop and n-loop homoclinic orbits, respectively.
8. *Map (41) has stable fixed point $d_{hn} = 1$ that corresponds to the strange Lorenz-type attractor in master map (40) and piecewise-smooth system (1). An infinite sequence of multi-loop homoclinic bifurcations leading to the emergence of the Lorenz-type attractor*

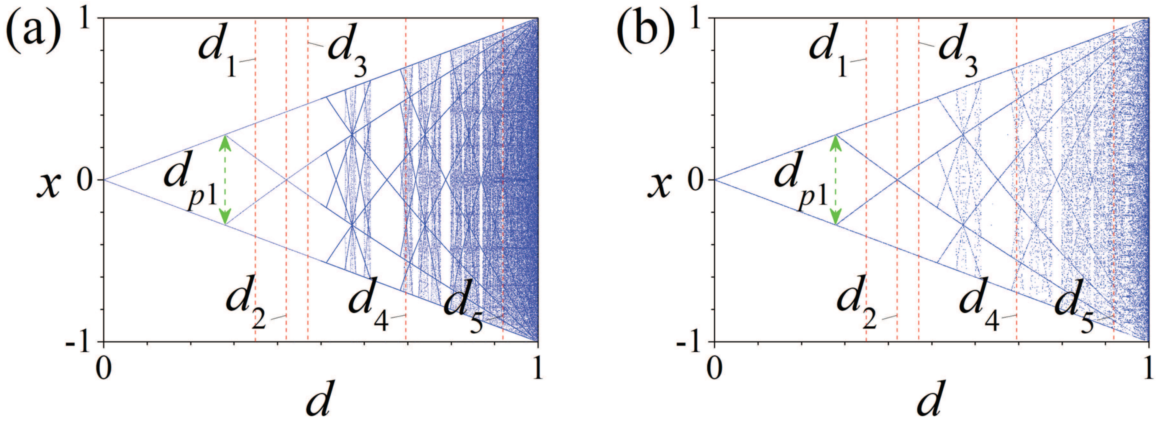

FIG. 8. Numerical validation of the route to chaos from Theorem 2. (a) 1D bifurcation diagram for master map (40) with $\nu = 0.8$ (b) 1D bifurcation diagram of system (1) obtained by numerically calculating flow trajectories and plotting their intersections with global cross section $z = b$. Range $\lambda \in [1.298, 0]$ with fixed $\nu = 0.8$, $\omega = 1$, $\alpha = 2$, $\delta = 0.588$ in (1) yields range $d \in [0, 1]$ in (40) via $d = 2\sqrt{1 + \frac{\lambda}{\omega}^2} \exp(-\frac{\lambda}{\omega} \arctan \frac{\lambda}{\omega}) - 1$. The first homoclinic bifurcation at $d = d_{h1} = 0$ gives birth to a stable period-2 orbit that undergoes a pitchfork bifurcation at $d = d_{p1} = 0.279$ (the green double end arrow) to become unstable and induce two stable period-2 orbits. Further increasing d generates a cascade of alternating homoclinic and pitchfork bifurcations that leads to the formation of the strange Lorenz-type attractor at $d = 1$. Red dashed vertical lines at $d_1 = 0.35$, $d_2 = d_{h2} = 0.4204$, $d_3 = 0.47$, $d_4 = 0.696$, $d_5 = 0.91906$, and $d_6 = 1$ (not shown) correspond to phase portraits in Fig. 9.

and accumulating toward the limiting value $d = 1$ has the scaling factor

$$\Delta = \lim_{n\to\infty} \frac{d_{hn} - d_{h(n-1)}}{d_{h(n-1)} - d_{h(n-2)}} = \frac{1}{2\nu}. \tag{42}$$

This scaling factor represents the limiting ratio of each bifurcation interval between subsequent homoclinic bifurcations to the next interval in the vicinity of $d = 1$ at the edge of chaos.

Proof. The proof of Claims 1–3 is similar to that of Theorem 2 and follows from a straightforward analysis of fixed points in master map (40). Equation $2d^\nu + d = 1$ for determining $d = d_{p1}$ in Claim 4 appears from the requirement for the pitchfork bifurcation to place the image of point $x = (\frac{1-d}{2})^{\frac{1}{\nu}}$, at which the sliding (horizontal fragment) and non-sliding parts of graph of $f(x)$ meet each other, at line $\bar{x} = -x$ [Fig. 6(d)]. The superstability of the two symmetrical period orbits appeared at $d > d_1$ [Fig. 6(e)] is guaranteed by the horizontal slope of the sliding fragments in the graph of $f(x)$.

The value $d = d_{h2} = \left(\frac{1}{2}\right)^{\frac{1}{\nu}}$ in Claim 5 comes from the requirement for the image of point $x = -(\frac{1-d}{2})^{\frac{1}{\nu}}$, $\bar{x} = d_{h2}$, to be further mapped into the right x intercept of $f(x)$ to form a period-2 homoclinic orbit. This yields $0 = -1 + 2d_{h2}^\nu$ and, therefore, $d_{h2} = \left(\frac{1}{2}\right)^{\frac{1}{\nu}}$.

The proof of Claim 6 is similar to that of Claim 3. The equation for finding d_{p2} is a particular case of recursive formula (41) in Claim 7, which is in turn derived from the inverse master map $x = f^{-1}(\bar{x})$. This inverse map is used to find pre-images of singularity point $x = 0$ that corresponds to a homoclinic orbit. If for a given value of d a pre-image of $x = 0$ falls on the horizontal fragment $\bar{x} = f(x) = d$, a stable homoclinic orbit is formed. The number of subsequent pre-images it takes the point $x = 0$ to be mapped back into itself amounts to the number of loops in the homoclinic orbit. Each $(n + 1)$-loop homoclinic orbit is formed by adding one additional step (pre-image) to the cobwebbing of an n-loop homoclinic orbit [see the formation of the two-loop, three-loop, and four-loop homoclinic orbits in Fig. 6(f)]. Therefore, it is sufficient to substitute the preimage $\bar{x} = d_{hn}$ into the inverse master map $x = f^{-1}(\bar{x}) = \left(\frac{\bar{x}+1}{2}\right)^{\frac{1}{\nu}}$ that has to be equal to $x = d_{h(n+1)}$ for the subsequent $(n + 1)$-loop homoclinic orbit. This yields recursive formula (41).

Finally, we need to derive the scaling factor Δ in Claim 8. Note that recursive formula (41) is a map with fixed point $d_{hn} = 1$. Remarkably, for $d = d_{hn} = 1$, the master map (40) turns into map

$$\bar{x} = (-1 + 2|x|^\nu)\operatorname{sign} x \tag{43}$$

that represents the standard Lorenz map with the strange Lorenz attractor without sliding motions. The fixed point $d_{hn} = 1$ of the map induced by the recursive formula (41) is stable since the derivative of $\chi(d_{hn})$ with respect to $d_{hn} : \chi'(d_{hn})|_{d_{hn}=1} = \frac{1}{2\nu} \in [\frac{1}{2}, 1) < 1$. Therefore, $d_{hn} \to 1$ for $n \to \infty$ and represents an infinite sequence of multi-loop homoclinic bifurcations, leading to the emergence of the Lorenz-type attractor. Note that the derivative $\chi'(d_{hn})|_{d_{hn}=1}$ can be represented by the difference quotient $\frac{d_{hn}-d_{h(n-1)}}{d_{h(n-1)}-d_{h(n-2)}} = \frac{1}{2\nu}$ that yields the scaling factor in Claim 8. □

Remark 5. Claims 1–3 of Theorem 2 describe a sliding homoclinic bifurcation of saddle O_s with a positive saddle value that is different from the non-classical bifurcation detailed in Theorem 1. The new feature is that two stable limit cycles merge into the homoclinic orbit at the bifurcation, rendering it stable (Fig. 7). In contrast to the non-classical bifurcation of Theorem 1, the positive sign of the saddle value is no longer informative in this case as the homoclinic orbit has to contain a non-negligible part of stable sliding motions

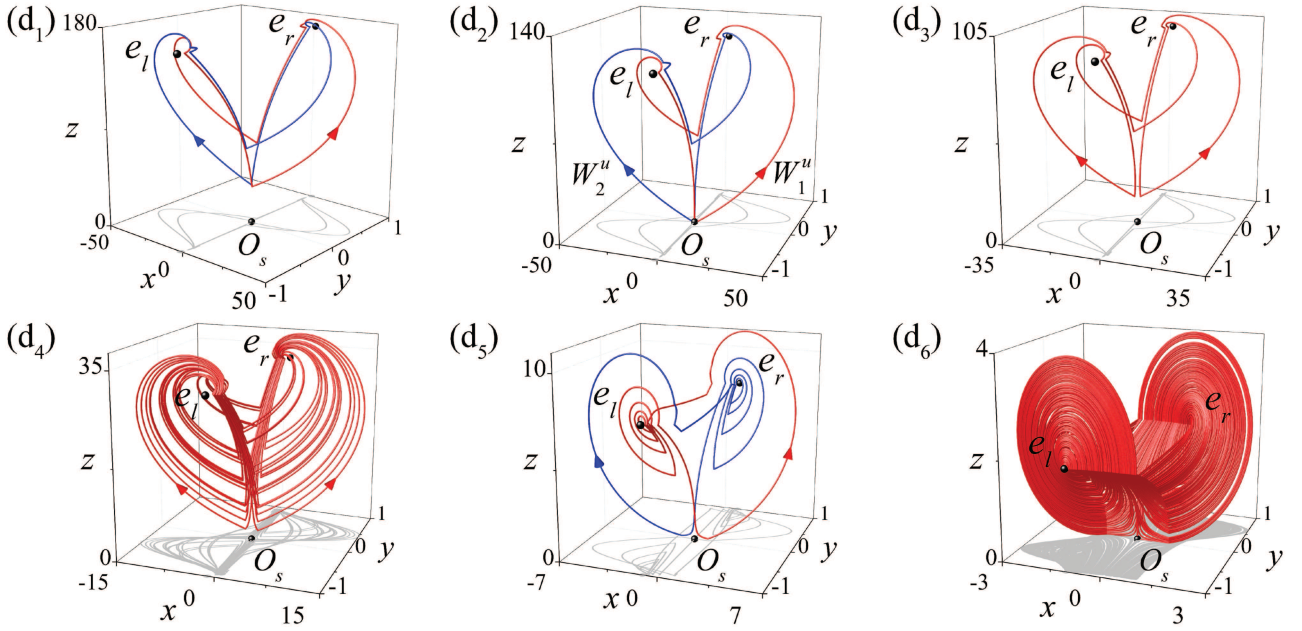

FIG. 9. Phase portraits of system (1) corresponding to $d = d_1, d_2, d_3, d_4, d_5, d_6$ in Fig. 8. (d_1) Two stable period-2 limit cycles (blue and red). $\lambda = 0.941$ ($d = 0.35$). (d_2) Four-loop homoclinic orbit. $\lambda = 0.8714$ ($d = 0.4204$). (d_3) Stable period-4 limit cycle born from the homoclinic orbit in (d_2). $\lambda = 0.823$ ($d = 0.47$). (d_4) Typical stable long-period orbit. $\lambda = 0.5895$ ($d = 0.696$). (d_5) Two symmetrical long-period stable orbits. $\lambda = 0.2894$ ($d = 0.919\,06$). (d_6) Strange Lorenz-type attractor without sliding motions. $\lambda = 0$ ($d = 1$). Other parameters are as in Fig. 8.

to make the homoclinic orbit stable and outweigh its local instability near the saddle.

Theorem 2 suggests a route to chaos in piecewise-smooth system (1) via alternating multi-loop homoclinic bifurcations and pitchfork bifurcations of stable periodic orbits (see Figs. 8 and 9). Each homoclinic butterfly bifurcation leads to the emergence of a stable orbit with double the period of the original orbits that merge into the homoclinic butterfly and disappear. It is then followed by a supercritical pitchfork bifurcation that renders the orbit unstable and creates two stable orbits with the period of its predecessor. With some caveats due to sliding motions, this replicating bifurcation sequence displays scaling self-similarity typical for cascades of period-doubling bifurcation.[65] Our bifurcation transition to chaos is similar to the ones described previously in smooth Lorenz-type systems[60,61] where pitchfork bifurcations are followed by bifurcations of stable multi-loop homoclinic orbits. Specific to our bifurcation scenario are (i) a positive saddle value, (ii) chaotic windows with discontinuity-induced homoclinic and heteroclinic bifurcations impossible in smooth systems, and (iii) an analytical description of the bifurcation cascade with a possibility of giving explicit parameter values for the principal homoclinic bifurcations.

While the analytical derivation of master map (37) and, therefore, of its special case (40) guarantees a rigorous one-to-one correspondence between the dynamics of master map (37) and generating piecewise-smooth system (1), we provide additional evidence by comparing bifurcation diagrams for master map (37) and for piecewise-smooth system (1) (Fig. 8). These two diagrams coincide to the highest degree allowed by the constraints imposed by numerical simulations. Different densities of trajectories in the two diagrams are due to different integration times. Figure 10 gives an overall picture of the bifurcations described in this paper and relates them to each other and to the parameter region where the strange Lorenz-type attractor exists.

By reversing the order of the bifurcation transition in Theorem 2 from $d = 1$ to $d = 0$, we can analytically characterize the destruction of the strange Lorenz-type attractor without sliding motions[7] existing in piecewise-smooth system (1) at $d = 1$. Our analysis of accumulating homoclinic and pitchfork bifurcations in the vicinity of $d = 1$ indicates that perturbations of $d = 1$ that induce stable sliding motions cause the explosion of infinitely many homoclinic and pitchfork bifurcations. These bifurcations in turn give birth to stable long-period orbits with arbitrarily small basins of attraction, turning the strange Lorenz-type attractor into a quasiattractor.[66] In terms of 1D master map (38), this transition is caused by the emergence of infinitesimal horizontal fragments in the graph of the map's function, which leads to the collapse of the corresponding x intervals into two points. Although it has a different origin due to stable sliding motions, this transition can be viewed as an analog of the destruction mechanism for the Lorenz attractor in the Lorenz map[45] beyond the foliation condition[46,57,58] through the appearance of Smale horseshoes.

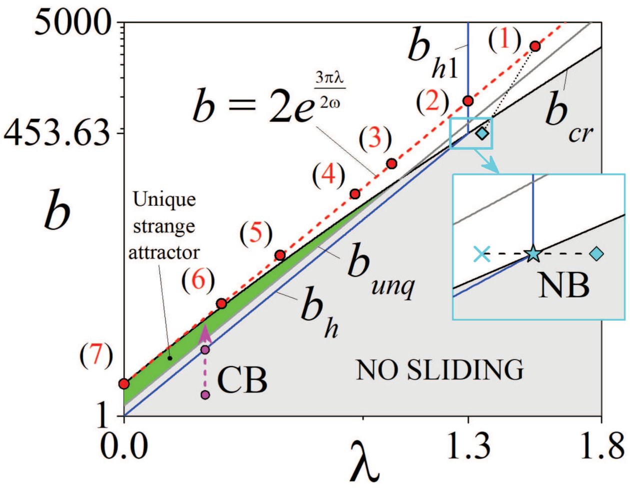

FIG. 10. 2D bifurcation diagram that relates the classical homoclinic bifurcation (CB), the non-classical bifurcation (NB) of Theorem 1 to the bifurcation transition of Theorem 2 and parameter regions with non-sliding dynamics. Black curve b_{cr} defined in (10) separates the regions with sliding (white) and no sliding (green and gray). Curve b_h : $b = \exp \frac{3\pi\lambda}{2\omega}$ and vertical line b_{h1} form the blue boundary that corresponds to homoclinic bifurcations in the absence and presence of sliding, respectively. Gray line b_{unq} : $b = \frac{1}{\nu} \exp \frac{3\pi\lambda}{2\omega}$ corresponds to the loss of stability of foci $e_{r,l}$ via an Andronov–Hopf-like bifurcation (see Ref. 7 for the details) that makes the strange Lorenz-type attractor existing in the no-sliding region a unique attracting set (green area). Vertical dashed purple arrow CB exemplifies the classical bifurcation (CB) transition detailed in Subsection IV A. The inset illustrates the non-classical bifurcation (NB) of Theorem 1 and indicates the transition from Fig. 5(a) (diamond) to Fig. 5(c) (cross) through Fig. 5(b) (asterisk) with parameters $\lambda = 1.298\,127$, $b = 453.629$. The red dashed line displays the route to chaos of Theorem 2 from two stable cycles to the strange attractor. The points (red circles) have the following correspondence: (1) Fig. 6(a), (2) Fig. 6(b), (3) Fig. 6(d), (4) Fig. 6(f) and Fig. 9(d_2), (5) Fig. 9(d_4), (6) Fig. 2(c), and (7) Fig. 9(d_6). The black dotted line connecting the diamond and point (1) exemplifies a route from two stable foci in the absence of sliding (diamond) via the homoclinic butterfly with sliding tangency (asterisk) to two stable limit cycles with sliding [point (1)]. Other parameters are $\omega = 1$, $\nu = 0.8$, $\delta = 0.588$, $\alpha = 2$.

VI. CONCLUSIONS

Rigorous computer-free studies of the birth, evolution, and disappearance of chaotic attractors in smooth systems are impaired by the absence of closed-form solutions and often remain elusive. Piecewise-smooth dynamical systems that partition phase spaces into regions that are governed by different linear differential equations can offer analytical insights into global bifurcations that create or destroy a chaotic attractor. Using non-smooth systems comes with a cost since many standard tools and classical theorems from bifurcation theory of smooth systems may be ill-suited for non-smooth systems. For example, non-smooth systems can exhibit global bifurcations that are drastically different from their smooth analogs, thereby requiring the development of non-smooth global bifurcation theory.

In this paper, we made significant progress toward characterizing the underpinnings of such sliding homoclinic bifurcations in piecewise-smooth dynamical systems. We considered a piecewise-smooth Lorenz-type system[7] with closed-form solutions to analytically describe novel types of sliding homoclinic bifurcations in which unstable homoclinic orbits can generate stable periodic orbits. In particular, we proved that the emergence of an infinitesimal part of stable sliding motions in an otherwise unstable homoclinic orbit can give birth to a stable periodic orbit. This was done by deriving an analytically tractable Poincaré return map that accounts for the presence of sliding motions. Our analysis of this map that turns into the classical 1D Lorenz map in the absence of sliding motions revealed distinct non-classical bifurcation scenarios by which the homoclinic butterfly can induce stability.

We also characterized sequences of alternating homoclinic butterfly and pitchfork bifurcations that lead to the formation or destruction of a strange Lorenz-type attractor whose existence in the absence of sliding motions was rigorously proved in our previous paper.[7] Here, we showed that the emergence of any small sliding segment in the attractor's trajectories can lead to the explosion of its bifurcation set via the emergence of infinitely many stable long-period orbits.

We expect our non-classical sliding homoclinic bifurcations to manifest in other non-smooth systems. We conjecture that for such non-classical bifurcations to appear in a piecewise-smooth system, it is necessary for the system's switching manifold to have a component that is parallel to the stable manifold of the saddle fixed point. In our piecewise-smooth system, the sliding manifold (plane) is strictly parallel to the stable manifold of the saddle, thereby maximizing the impact of stable sliding motions.

Our rigorous description of sliding homoclinic bifurcations of a saddle can also be applied to find and characterize similar non-classical analogs of Shilnikov saddle-focus homoclinic bifurcations in piecewise-smooth dynamical systems. Potential candidates include a possible piecewise-smooth version of the Rössler system[67] that can be built using our geometrical method of constructing an analytically tractable piecewise-smooth dynamical system with a predefined chaotic attractor.[7]

At a more general level, our study contributes to articulating the constructive role of non-smoothness in stabilizing and controlling smooth systems. Examples include the emergence of stable ghost attractors[68–70] and windows of opportunity for synchronization[71–73] in switched systems and improved performance of impacting mechanical systems.[10,16]

ACKNOWLEDGMENTS

This work was supported by the Ministry of Science and Higher Education of the Russian Federation under Grant No. 0729-2020-0036, by the Russian Science Foundation under Grant No. 19-12-00367 (numerics; to V.N.B. and N.V.B.), and by the National Science Foundation (NSF) (USA) under Grant Nos. DMS-1909924 and CMMI-2009329 (to I.V.B.).

DATA AVAILABILITY

The data that support the findings of this study are available from the corresponding author upon reasonable request.

REFERENCES

[1] J. Guckenheimer and P. Holmes, *Nonlinear Oscillations, Dynamical Systems, and Bifurcations of Vector Fields* (Springer, 1983), Vol. 42.
[2] L. P. Shilnikov, A. L. Shilnikov, D. V. Turaev, and L. Chua, *Qualitative Theory in Nonlinear Dynamics. Part II* (World Scientific, 2001).
[3] A. J. Homburg and B. Sandstede, *Handbook of Dynamical Systems* (North-Holland Amsterdam, 2010), Vol. 3, pp. 379–524.
[4] Y. A. Kuznetsov, *Elements of Applied Bifurcation Theory* (Springer Science & Business Media, 2013), Vol. 112.
[5] L. P. Shilnikov, Dokl. Akad. Nauk **160**, 558 (1965).
[6] L. P. Shilnikov, Mat. USSR Sb. **77**(119), 461 (1968).
[7] V. N. Belykh, N. V. Barabash, and I. V. Belykh, Chaos **29**, 103108 (2019).
[8] A. A. Andronov, A. A. Vitt, and S. E. Khaikin, *Theory of Oscillations* (Fizmatgiz, Moscow, 1959).
[9] A. Filippov, *Differential Equations with Discontinuous Right-Hand Sides* (Kluwer Academic Press, 1988).
[10] M. di Bernardo, C. Budd, A. Champneys, and P. Kowalczyk, *Piecewise-Smooth Dynamical Systems: Theory and Applications* (Springer, 2007).
[11] M. di Bernardo, M. I. Feigin, S. J. Hogan, and M. E. Homer, Chaos, Solitons Fractals **10**, 1881 (1999).
[12] R. I. Leine and H. Nijmeijer, in *Dynamics and Bifurcations of Non-smooth Mechanical Systems* (Springer, 2004), pp. 125–176.
[13] J. H. Macdonald, Proc. R. Soc. London Ser. A **465**, 1055 (2008).
[14] I. V. Belykh, R. Jeter, and V. N. Belykh, Chaos **26**, 116314 (2016).
[15] I. Belykh, R. Jeter, and V. Belykh, Sci. Adv. **3**, e1701512 (2017).
[16] L. Serdukova, R. Kuske, and D. Yurchenko, Nonlinear Dyn. **98**, 1807 (2019).
[17] N. Gubar′, J. Appl. Math. Mech. **25**(6), 1011–1023 (1961).
[18] T. Matsumoto, L. Chua, and M. Komoro, Physica D **24**, 97 (1987).
[19] L. Benadero, A. El Aroudi, G. Olivar, E. Toribio, and E. Gomez, Int. J. Bifurcat. Chaos **13**, 427 (2003).
[20] D. J. Simpson, S. J. Hogan, and R. Kuske, SIAM J. Appl. Dyn. Syst. **12**, 533 (2013).
[21] A. Polynikis, S. Hogan, and M. di Bernardo, J. Theor. Biol. **261**, 511 (2009).
[22] V. Acary, H. De Jong, and B. Brogliato, Physica D **269**, 103 (2014).
[23] B. Ermentrout, Y. Park, and D. Wilson, Philos. Trans. R. Soc. A **377**, 20190092 (2019).
[24] A. R. Champneys and M. di Bernardo, Scholarpedia **3**, 4041 (2008).
[25] Z. T. Zhusubaliyev and E. Mosekilde, *Bifurcations and Chaos in Piecewise-Smooth Dynamical Systems*, World Scientific Series on Nonlinear Science Series A Vol. 44 (World Scientific, 2003).
[26] H. E. Nusse, E. Ott, and J. A. Yorke, Phys. Rev. E **49**, 1073 (1994).
[27] M. di Bernardo, C. J. Budd, A. R. Champneys, P. Kowalczyk, A. B. Nordmark, G. O. Tost, and P. T. Piiroinen, SIAM Rev. **50**, 629 (2008).
[28] A. C. Luo and B. Xue, Int. J. Bifurcat. Chaos **19**, 2165 (2009).
[29] L. Dieci and L. Lopez, SIAM J. Numer. Anal. **47**, 2023 (2009).
[30] Y. A. Kuznetsov, S. Rinaldi, and A. Gragnani, Int. J. Bifurcat. Chaos **13**, 2157 (2003).
[31] D. Simpson and J. Meiss, SIAM J. Appl. Dyn. Syst. **7**, 795 (2008).
[32] R. Szalai and H. M. Osinga, SIAM J. Appl. Dyn. Syst. **8**, 1434 (2009).
[33] A. Colombo and F. Dercole, SIAM J. Appl. Dyn. Syst. **9**, 62 (2010).
[34] D. Simpson, Phys. Lett. A **382**, 2439 (2018).
[35] H. E. Nusse and J. A. Yorke, Physica D **57**, 39 (1992).
[36] M. Feigin, J. Appl. Math. Mech. **34**, 822 (1970).
[37] M. di Bernardo, M. Feigin, S. Hogan, and M. Homer, Chaos, Solitons Fractals **11**, 1881 (1999).
[38] M. di Bernardo and S. Hogan, Philos. Trans. R. Soc. A **368**, 4915 (2010).
[39] K. Lu, Q. Yang, and G. Chen, Chaos **29**, 043124 (2019).
[40] D. D. Novaes and M. A. Teixeira, Chaos **29**, 063110 (2019).
[41] P. Glendinning, Eur. J. Appl. Math. **29**, 757 (2018).
[42] W. Tucker, C. R. Acad. Sci. Ser. I: Math. **328**, 1197 (1999).
[43] I. I. Ovsyannikov and D. V. Turaev, Nonlinearity **30**, 115 (2017).
[44] V. S. Afraimovich, V. V. Bykov, and L. P. Shilnikov, Akad. Nauk SSSR Dokl. **234**, 336 (1977).
[45] C. Sparrow, *The Lorenz Equations: Bifurcations, Chaos and Strange Attractors* (Springer, 1982).
[46] V. V. Bykov and A. L. Shilnikov, Sel. Math. Sov. **11**, 375–382 (1992).
[47] R. Barrio, A. Shilnikov, and L. Shilnikov, Int. J. Bifurcat. Chaos **22**, 1230016 (2012).
[48] E. J. Doedel, B. Krauskopf, and H. M. Osinga, Nonlinearity **19**, 2947 (2006).
[49] E. J. Doedel, B. Krauskopf, and H. M. Osinga, Nonlinearity **28**, R113 (2015).
[50] D. Viswanath, Nonlinearity **16**, 1035 (2003).
[51] B. Hassard, J. Zhang, S. Hastings, and W. Troy, Appl. Math. Lett. **7**, 79 (1994).
[52] Z. Galias and P. Zgliczyński, Physica D **115**, 165 (1998).
[53] M. Breden and J.-P. Lessard, Discrete Contin. Dyn. Syst. B **23**, 2825 (2018).
[54] K. Mischaikow and M. Mrozek, Bull. Am. Math. Soc. **32**, 66 (1995).
[55] B. Hassard and J. Zhang, SIAM J. Math. Anal. **25**, 179 (1994).
[56] W. D. Kalies, S. Kepley, and J. D. Mireles James, SIAM J. Appl. Dyn. Syst. **17**, 157 (2018).
[57] A. L. Shilnikov, Physica D **62**, 338 (1993).
[58] J. L. Creaser, B. Krauskopf, and H. M. Osinga, SIAM J. Appl. Dyn. Syst. **16**, 2127 (2017).
[59] V. N. Belykh, N. V. Barabash, and I. V. Belykh, Autom. Remote Control **81**, 1385 (2020).
[60] A. Arneodo, P. Coullet, and C. Tresser, Phys. Lett. A **81**, 197 (1981).
[61] D. Lyubimov and M. Zaks, Physica D **9**, 52 (1983).
[62] E. Lorenz, J. Atmos. Sci. **20**, 130 (1963).
[63] C. Robinson, Nonlinearity **2**, 495–518 (1989).
[64] C. Robinson, SIAM J. Math. Anal. **23**, 1255–1268 (1992).
[65] M. J. Feigenbaum, J. Stat. Phys. **19**, 25 (1978).
[66] S. Gonchenko, L. Shilnikov, and D. Turaev, Chaos **6**, 15 (1996).
[67] O. E. Rössler, Phys. Lett. A **57**, 397 (1976).
[68] I. Belykh, V. Belykh, R. Jeter, and M. Hasler, Eur. Phys. J. Spec. Top. **222**, 2497 (2013).
[69] M. Hasler, V. Belykh, and I. Belykh, SIAM J. Appl. Dyn. Syst. **12**, 1031 (2013).
[70] N. V. Barabash, T. A. Levanova, and V. N. Belykh, Chaos **30**, 081105 (2020).
[71] R. Jeter and I. Belykh, IEEE Trans. Circuits Syst. I: Regul. Pap. **62**, 1260 (2015).
[72] O. Golovneva, R. Jeter, I. Belykh, and M. Porfiri, Physica D **340**, 1 (2017).
[73] R. Jeter, M. Porfiri, and I. Belykh, Chaos **28**, 071104 (2018).